


## Article

# Long-Term Spatiotemporal Variation of Droughts in the Amazon River Basin

Franklin Paredes-Trejo <sup>1,2,\*</sup>, Humberto Alves Barbosa <sup>2</sup>, Jason Giovannettone <sup>3</sup>, T. V. Lakshmi Kumar <sup>4</sup>, Manoj Kumar Thakur <sup>5</sup> and Catarina de Oliveira Buriti <sup>6</sup>

- <sup>1</sup> Department of Civil Engineering, San Carlos Campus, University of the Western Plains Ezequiel Zamora, San Carlos 2201, Venezuela
- <sup>2</sup> Laboratório de Análise e Processamento de Imagens de Satélites (LAPIS), Instituto de Ciências Atmosféricas, A. C. Simões Campus, Universidade Federal de Alagoas, Alagoas 57072-900, Brazil; barbosa33@gmail.com
- <sup>3</sup> Dewberry, 8401 Arlington Blvd., Fairfax, VA 22031, USA; jggiovannettone@gmail.com
- <sup>4</sup> Atmospheric Science Research Laboratory, SRM University, Kattankulathur 603203, India; lkumarap@hotmail.com
- <sup>5</sup> Department of Physics, Tribhuvan University, Kathmandu 44600, Nepal; thakurmanoj2003@yahoo.com
- <sup>6</sup> National Semi-Arid Institute (INSA), Ministry of Science, Technology, Innovations and Communications (MCTIC), Campina Grande 58100-000, Brazil; catarinaburiti@gmail.com
- \* Correspondence: franklinparedes75@gmail.com; Tel.: +58-258-2517-675

**Abstract:** The Amazon River Basin (ARB) plays an important role in the hydrological cycle at the regional and global scales. According to the Intergovernmental Panel on Climate Change (IPCC), the incidence and severity of droughts could increase in this basin due to human-induced climate change. Therefore, the assessment of the impacts of extreme droughts in the ARB is of vital importance to develop appropriate drought mitigation strategies. The purpose of this study is to provide a comprehensive characterization of dry spells and extreme drought events in terms of occurrence, persistence, spatial extent, severity, and impacts on streamflow and vegetation in the ARB during the period 1901–2018. The Standardized Precipitation–Evapotranspiration Index (SPEI) at multiple time scales (i.e., 3, 6, and 12 months) was used as a drought index. A weak basin-wide drying trend was observed, but there was no evidence of a trend in extreme drought events in terms of spatial coverage, intensity, and duration for the period 1901–2018. Nevertheless, a progressive transition to drier-than-normal conditions was evident since the 1970s, coinciding with different patterns of coupling between the El Niño/Southern Oscillation (ENSO) phenomenon and the Pacific Decadal Oscillation (PDO), Atlantic Multidecadal Oscillation (AMO), and Madden–Julian Oscillation (MJO) as well as an increasing incidence of higher-than-normal surface air temperatures over the basin. Furthermore, a high recurrence of short-term drought events with high level of exposure to long-term drought conditions on the sub-basins Ucayali, Japurá–Caquetá, Jari, Jutai, Marañón, and Xingu was observed in recent years. These results could be useful to guide social, economic, and water resource policy decision-making processes in the Amazon basin countries.

**Keywords:** Amazonia; drought; Amazon river basin; SPEI



**Citation:** Paredes-Trejo, F.; Barbosa, H.A.; Giovannettone, J.; Lakshmi Kumar, T.V.; Thakur, M.K.; de Oliveira Buriti, C. Long-Term Spatiotemporal Variation of Droughts in the Amazon River Basin. *Water* **2021**, *13*, 351. <https://doi.org/10.3390/w13030351>

Academic Editor: Achim A. Beylich  
Received: 14 December 2020  
Accepted: 27 January 2021  
Published: 30 January 2021

**Publisher's Note:** MDPI stays neutral with regard to jurisdictional claims in published maps and institutional affiliations.



**Copyright:** © 2021 by the authors. Licensee MDPI, Basel, Switzerland. This article is an open access article distributed under the terms and conditions of the Creative Commons Attribution (CC BY) license (<https://creativecommons.org/licenses/by/4.0/>).

## 1. Introduction

The Amazon River Basin (ARB) is the largest water basin in the world and a dynamic ecosystem that flows through Brazil, Peru, Bolivia, Colombia, Ecuador, Venezuela, Guyana, and Suriname [1]. It is also the largest rainforest in the world [2]. Approximately 2/3rd of the ARB includes the states of Acre, Amazonas, Santa Catarina, Rondônia, and Roraima and part of the states of Amapá, Mato Grosso, and Pará in Brazil [3]. In the northern ARB, the below-normal rainfall and streamflow are often linked to El Niño–Southern Oscillation (ENSO) conditions in the tropical Pacific [4–6], sea surface temperature (SST) anomalies in the tropical Atlantic [7,8], or to an interaction of both at different time scales [4,9,10].

The ARB suffered two unprecedented drought events in 2005 and 2010. In the case of 2005, large regions of the western ARB were affected by elevated warming in the tropical North Atlantic and reported one of the most severe droughts of the previous 100 years. Unlike the drought episode of 2005, the 2010 event was preceded by anomalous warming over the equatorial Pacific and North Atlantic oceans [4,11,12].

Throughout history, droughts have caused strong social, economic, and environmental impacts in the ARB [13], which are exacerbated by anthropogenic factors such as land use changes associated with the agriculture and forestry sectors [4]. During the last two decades, several studies have revealed a recurrent delay in the onset of the rainy season and drought conditions over different regions of the ARB [1,13], mostly driven by the impact of global climate change on the moisture transport from the tropical north Atlantic [14,15] and the ENSO phenomenon [8]. In line with these findings, the Fourth Assessment Report (AR4) of the Intergovernmental Panel on Climate Change (IPCC) warned that the dry spells and droughts have been worsening in recent years over the ARB [16]. Climate change projections used in the IPCC Fifth Assessment Report (AR5-IPCC) also show an intensification of dry spells and droughts for the 21st century [17–19]. The intensification of drought conditions in the ARB is receiving increasing attention among water resource managers, farmers, development specialists, researchers, and policy makers [20], due to the negative implications for biodiversity, water resource management, food security, transportation, rainfed agriculture, and native people.

The simplest way for monitoring drought conditions is to use drought indices, which provide traceable information on intensity, severity, and duration [21]. Nevertheless, this approach has limitations when applied to large regions with scarce ground-based climate data because it cannot offer reliable information on drought conditions. With recent advances in remote sensing, most of the drought indices can be calculated in areas where ground-based data are sparse using remote sensing data, such as the Standardized Precipitation Evapotranspiration Index (SPEI) [22], Standardized Precipitation Index (SPI) [23,24], Normalized Difference Vegetation Index (NDVI) [13], Enhanced Vegetation Index (EVI) [25], among others. Satellite-based drought indices have recently become an alternative for monitoring drought risks in large and sparsely-gauged areas similar to the ARB [26].

The SPEI has been widely used to assess drought impacts in different parts of the world [27–29] due to its multi-scalar nature, its capacity to identify different drought types (i.e., meteorological, hydrological, and agricultural), and its sensitivity to long-term trends in temperature change [22,30]. The SPEI takes into account the difference between the precipitation (P) and potential evapotranspiration (PET) at different time scales, which is fitted with a probability distribution for a baseline period. The fitted values are then standardized and classified into drought categories [22,28].

Unlike the SPEI, the NDVI is a drought index based on the ratio of spectral reflectance values of red and near-infrared bands derived from optical sensors on board of satellite platforms [31]. The NDVI is widely used for agricultural drought monitoring, due to its remarkable sensitivity to the condition of the vegetation [32] as well as precipitation and soil moisture [13]. Nevertheless, the NDVI exhibits a noticeable effect of saturation over high biomass areas [33]. The EVI is proposed to overcome this limitation of the NDVI, which, in addition to red and near-infrared bands, uses the values of reflectance from the blue band to minimize atmospheric and soil background effects [25].

Numerous studies conducted in the ARB have focused on the main characteristics of drought events of 2005 [7,11,34] and 2010 [11,35]. In some studies, the NDVI was adopted as a drought index to assess the impact of drought conditions on vegetation during the occurrence of extreme events [13,36,37]. Similarly, the EVI was used to characterize the 2005 and 2010 droughts in Amazonia [38,39]. However, despite the advantages of SPEI over other drought indices, such as its flexibility to reflect the impact of droughts on different time scales, operational simplicity, and its probabilistic nature [28], very few studies have used the SPEI to assess drought impacts in the ARB. For example, Sorí et al. [40] used the SPEI at 1-, 6-, and 12-month time scales (i.e., SPEI1, SPEI6, and SPEI12, respectively) derived

from ground-based climate data to investigate the moisture uptake anomalies during the most intense wet and drought episodes in the Negro River and Madeira sub-basins from 1980 to 2016. They found that drought conditions within both sub-basins do not occur simultaneously, confirming that the climatic water balance may greatly differ within the ARB. Spinoni et al. [41] also used the SPEI3 and SPEI12 to identify drought episodes for the Amazon region defined by the AR5-IPCC during 1951–2016, but due to the fact that most of the climate networks currently available in the ARB are inadequate due to sparse spatial coverage, a high proportion of missing data, and short record lengths, the authors used P and PET from the Climatic Research Unit gridded Time Series (CRU TS) dataset [42]. They pointed out that the western Amazonia experienced increased drought frequency due to the progressive temperature increase in the last decades. Interestingly, to our knowledge, there is no recent study that assesses the long-term variability of extreme droughts through the SPEI over the entire ARB.

For the reasons exposed above, more detailed studies are still needed on the evolution of the dry spells and droughts to understand how climate variability could be affecting the distribution of extreme droughts in the ARB. This information is of paramount importance to develop appropriate strategies of planning and managing water resources during drought and water scarcity conditions. Thus, the objectives of this study are: (i) to evaluate the long-term temporal patterns of drought events in the entire ARB; (ii) to analyze the land–atmosphere coupling during the more recent extreme drought events in terms of their impacts on vegetation and streamflow; and (iii) to identify the regions of the ARB more prone to suffering drought events. The major novelty of this study with respect to similar previous studies is the use of the newest gridded global SPEI drought product based on the CRU TS dataset to delineate those areas of the ARB where drought events are becoming more frequent and persistent.

## 2. Materials and Methods

### 2.1. Study Area

The study was carried out over the Amazon River Basin (ARB), which is located between 5.3° N–20.1° S and 49.2–79.5° W (Figure 1a), with a drainage area of 4,670,000 km<sup>2</sup> at Óbidos on its mainstream [1] and an annual mean discharge of 163,000 m<sup>3</sup>/s [43]. The ARB has more than 24 million inhabitants and a human population density of about 4 inhabitants per square kilometer [44]. It is characterized by a vast range of biodiversity, landscapes, topography, climates, and rainfall regimes [45]. Roughly 43% of the ARB has a tropical rainforest climate [46]. Mean air temperature values range from 24 to 26 °C with an annual amplitude of 1 to 2 °C [15]. The mean annual precipitation across the ARB is approximately 2220 mm [47], ranging from around 1500 to >2500 mm [48] (Figure 1b). The temporal variability of precipitation is largely controlled by the moisture transport from the Atlantic Ocean [49], which in turn is modulated by SST anomalies over the tropical Atlantic region and the ENSO phenomenon [50], while the existence of a complex feedback between the climate and the forest has a significant control on its regional spatial variability [47,51]. Over the northern ARB, the rainy season occurs during March to May, whereas the dry season is from December to February. An opposite precipitation regime is observed in the southern ARB [49]. The ARB consists of 33 endorheic sub-basins (Figure 1c) [52]. The elevation of the ARB gradually rises from the eastern lowlands (near zero meters above sea level (a.s.l.)) to the higher Andes (above 5000 m a.s.l.) (Figure 1d) [53]. The forest is the most prominent land cover in the ARB and covers about 83% of its entire surface [54].

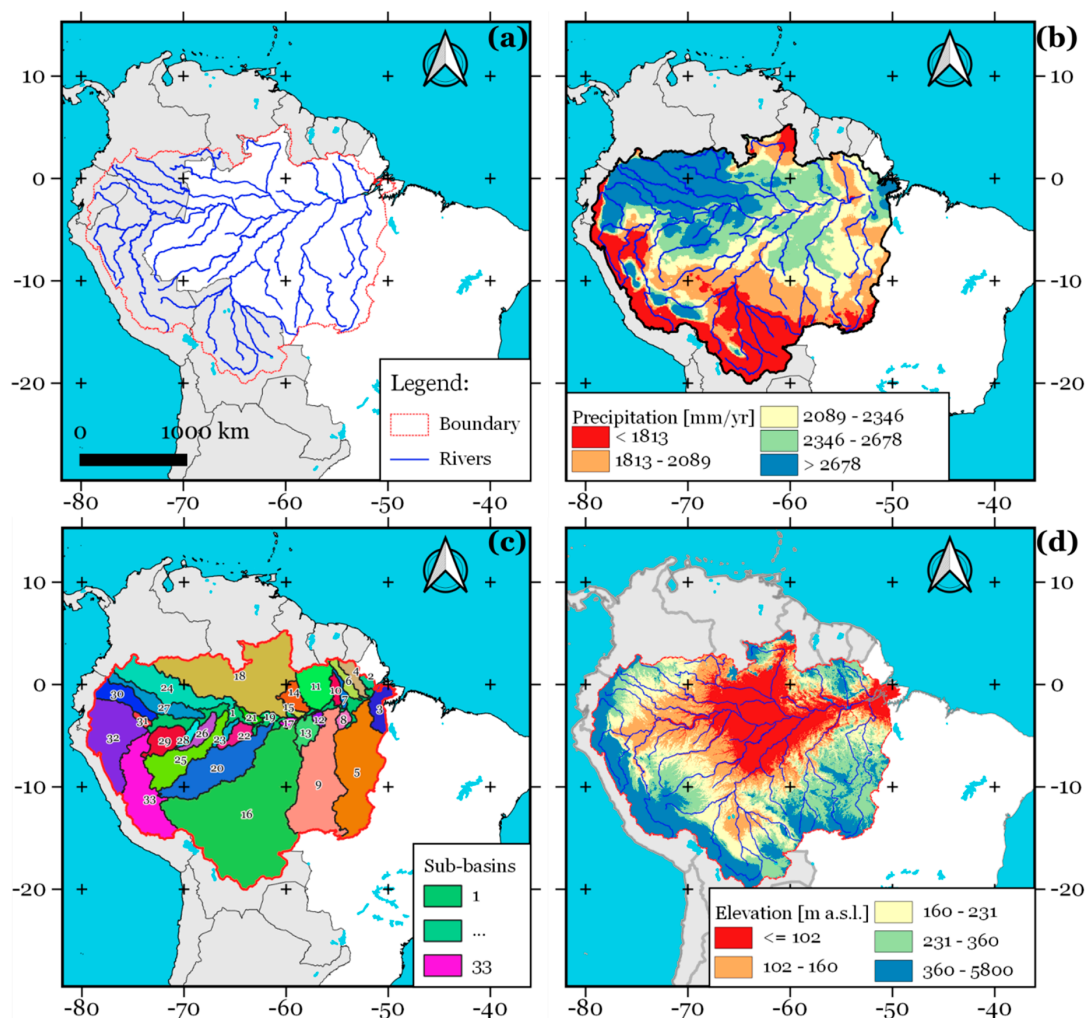


**Figure 1.** The study area: (a) the hydrographic network; (b) mean annual rainfall from the Climate Hazards Group InfraRed Precipitation with Stations (CHIRPS) [55] for the reference period 2000–2018; (c) sub-basins of the ARB according to Mayorga et al. [52] where 1, Amazonas-Solimões; 2, Macapá; 3, Marajó-Pará; 4, Jari; 5, Xingu; 6, Paru de Este; 7, Maicuru; 8, Curuá-Una; 9, Tapajós; 10, Curuá; 11, Trombetas-Nhamundá; 12, Mamuru; 13, Ilha Tupinambarana; 14, Uatumã; 15, Urubu; 16, Madeira; 17, Madeirinha; 18, Negro; 19, Manacapuru; 20, Purus; 21, Badajós; 22, Coari; 23, Tefé; 24, Japurá-Caquetá; 25, Juruá; 26, Jutaí; 27, Içá-Putumayo; 28, Jandiatuba; 29, Javari-Yavari; 30, Napo; 31, Nanay; 32, Marañón; and 33, Ucayali; (d) terrain elevation based on 250-m Digital Elevation Model—Shuttle Radar Topographic Mission (DEM-SRTM) images [56].

## 2.2. Datasets

### 2.2.1. Standardized Precipitation Evapotranspiration Index (SPEI)

The SPEI was used to assess drought conditions and their variability in time over the ARB. It was obtained from the Global SPEI database webpage (<https://spei.csic.es/database.html>; version 2.6 released in March 2020) at 3-, 6-, and 12-month time scales, respectively; covering January 1901 to December 2018. The rationale behind the choice of this dataset is related to the fact that the SPEI has a high sensitivity to temperature [28], good spatial coverage (global at 0.5° spatial resolution), and that it was recently updated by the Spanish National Research Council (CSIC). The 3-, 6-, and 12-month time scales were selected to focus attention on both short-term (i.e., SPEI3) and long-term (i.e., SPEI6 and SPEI12) drought events [22]. For the calculation of the SPEI, CSIC used P and PET from the newest CRU TS dataset (version 4.03), where the PET is based on the Food and Agriculture Organization of the United Nations-56 (FAO-56) Penman-Monteith formulation [57]. A large number of stations located in the ARB with good quality control and homogeneity checks were used by the Climatic Research Unit (University of East Anglia)

for the development of the CRU TS dataset [58]. Therefore, the SPEI dataset is considered a reliable dataset for drought studies, as confirmed in previous studies [28,41]. Moreover, the spatial and temporal consistency of the SPEI dataset was checked and their area-averaged time series were visually inspected to detect any problems. For more details about the SPEI dataset, the reader is referred to Vicente-Serrano et al. [28].

### 2.2.2. Enhanced Vegetation Index (EVI)

The EVI was used to assess the impact of drought conditions on vegetation in the ARB. The global gridded EVI data were obtained from the NASA Land Processes Distributed Active Archive Center (LP DAAC) webpage (<https://lpdaac.usgs.gov>), which derived this dataset from the MOD13C2 product (version 6.0) using a correction algorithm for molecular scattering, ozone absorption, and aerosols [59]. This dataset was selected because of its long temporal coverage (from 2000 to 2020), monthly aggregation, improved sensitivity over high biomass regions, moderate spatial resolution (0.05°), and the fact that it has been adopted for agricultural drought assessment in Amazonia [37]. Further details of the MOD13C2-based EVI dataset can be found in Solano et al. [59].

### 2.2.3. Ground-Based Observations

For the period 1974–2014 within the ARB, we used (Figure 1): (i) the monthly streamflow observations (in m<sup>3</sup>/s) from the Brazilian National Water Agency (ANA) streamflow gauge stations (available at <https://bit.ly/3eT3VJo>); and (ii) the monthly rainfall observations (in mm) from the National Institute of Meteorology (INMET) rain gauge stations (available at [www.inmet.gov.br](http://www.inmet.gov.br)). ANA and INMET apply a rigorous process of quality control and homogenization to these datasets before they are published. Data from both datasets are considered as reliable benchmarks against which to assess the performance of the SPEI in capturing drought conditions during the most recent drought events. In order to ensure a fair comparison of the drought conditions from the SPEI with ground-based data: (i) observations outside of the monthly mean  $\pm 3.5$  standard deviations (outlier values) under assumption of a Gaussian distribution [60] were coded as missing data; (ii) any observed time series with more than 10% missing data per month were omitted to maximize the reliability of the analyzes [61]; and (iii) missing data were not filled in to avoid the uncertainties inherent in the imputation techniques [62]. The result was that 13 streamflow gauge stations and 5 rainfall gauge stations passed these criteria and were, therefore, used in the following analyses.

### 2.2.4. Auxiliary Satellite-Based Datasets

The near-surface air temperature (T2M), land cover, climate type, terrain elevation, and rainfall were used as auxiliary information. The T2M was extracted from the re-analysis data of the European Centre for Medium-Range Weather Forecasts (ERA5) [63] at 0.25° spatial resolution for the period 1979–2018 (available online at <https://cds.climate.copernicus.eu>). The land cover data were obtained from the European Space Agency Land Cover-Climate Change Initiative (ESA LC-CCI) map of 2018 at 300 m spatial resolution (available online at <http://maps.elie.ucl.ac.be>) [64]. The climate type was extracted from the Köppen-Geiger climate classification developed by Beck et al. [46], which is available at <https://bit.ly/2Zt90Bu>. The elevation was derived from the Shuttle Radar Topographic Mission (SRTM) at 250 m spatial resolution (available online at <https://earthexplorer.usgs.gov>). The monthly rainfall dataset was derived from the Tropical Rainfall Measuring Mission (TRMM) Multi-satellite Precipitation Analysis (TMPA) 3B43v7 rainfall product [65] at 0.25° spatial resolution for the period 1998–2018. The rainfall data were retrieved from the web-based Geospatial Interactive Online Visualization and Analysis Infrastructure (Giovanni) application (available online at <https://giovanni.gsfc.nasa.gov>). Further information on the generation, validation, and calibration of these datasets is available in the links shown above.

### 2.3. Methodology

As a first step, all gridded datasets were clipped using a shapefile of the ARB as a mask while conserving their native spatial resolution to avoid the spatial uncertainty inherent in the interpolation techniques [66]. The clipped SPEI dataset at 1-, 6-, and 12-month time scales are provided in the Supplementary Materials.

For a given pixel and regardless of the time scale of the SPEI (i.e., 3-, 6-, or 12-month): (i) a dry spell starts when  $\text{SPEI} \leq -1.00$  during a period comprising at least two consecutive months, and it ends when  $\text{SPEI} > -1.00$ ; (ii) the duration of a dry spell is the number of months between its start and end; (iii) the peak is the lowest SPEI value during the occurrence of a dry spell; (iv) the severity is the absolute value of the sum of the values of SPEI from the start to end of the dry spell; (v) the intensity is the ratio between the severity and the duration of a dry spell, which is classified into one of the categories shown in Table 1.

**Table 1.** Drought categories for the values of SPEI following the criteria of Stage [67].

Class Names	SPEI
Extreme wet	>2.00
Severe wet	1.50 to 1.99
Moderate wet	1.00 to 1.49
Near normal	0.99 to −0.99
Moderate drought	−1.00 to −1.49
Severe drought	−1.50 to −1.99
Extreme drought	<−2.00

For a given month, the drought spatial coverage is the percentage of pixels with values of  $\text{SPEI} \leq -1.00$ . In this study, an extreme drought event occurs when the drought spatial coverage is greater than 20% (about 1,196,462 km<sup>2</sup>) for at least five consecutive months. The rationale behind the choice of this threshold is related to the fact that under this condition there are significant impacts on rainfall, vegetation, and water resources in the ARB [7,20], which can be detected in both the ground-based data and the satellite-based data [36,37]. During the occurrence of an extreme drought event, the persistence is the time period (as a percentage of the duration of the extreme drought event) in which a pixel shows values of  $\text{SPEI} \leq -1.00$ ; thus, this feature is a proxy for drought severity.

In a second step, the area-averaged values of SPEI via the median were used to explore the long-term temporal evolution of the drought conditions in the ARB in terms of its intensity and spatial coverage from 1901 to 2018 together with the identification of the onset and ending of extreme drought events. The median was chosen to minimize the bias effect of extreme values in both datasets [68]. The monthly intensity was calculated considering only those pixels where the  $\text{SPEI} \leq -1.00$ . The modified Mann–Kendall trend test, which is a non-parametric test developed by Yue and Wang [69] widely used to analyze trends in hydroclimatic time series regardless of the existence of serial correlation [70], was applied at the 5% significance level to verify the presence of long-term trends in the time series of SPEI3, SPEI6, SPEI12, along with the drought spatial coverage; the Theil–Sen method was applied to estimate the slope of said trends [71].

The extreme drought events were then analyzed in terms of their persistence and of any relationships that exist between the atmosphere, vegetation, and water resources. The coupling between the vegetation and atmosphere was examined by a wavelet coherence analysis (WCA) applied to the area-averaged values of SPEI against EVI, T2M, and TRMM-based rainfall during their common periods (i.e., 2001–2018, 1980–2018, and 1998–2018, respectively). The WCA is defined as the square of the cross-spectrum normalized by the individual power spectra; thus, unlike the linear correlation analysis, it allows temporal regions with high common power between two time series in time–frequency space to be revealed [72]. In this study, the computational procedure of the WCA described by Torrence and Compo [73] was used, while the Monte Carlo approach was used in the estimation of the level of statistical significance [74]. On the other hand, the coupling between the drought conditions and streamflow

was examined using both recent ground-based observations (i.e., rainfall and streamflow) and satellite-based data. The WCA was replaced in this case by a visual intercomparison because of the relatively short rainfall and streamflow periods of record.

Because drought episodes in terms of intensity, frequency, and duration can be exacerbated by local factors such as terrain characteristics and climate [7,34], a cluster analysis based on the k-medoids algorithm [75] was applied in order to better understand the extent of any potential relationships. The rationale behind the use of the k-medoids algorithm is that this is a robust approach to deal with both mixed-type data (i.e., nominal, ordinal and ordered) and outliers [75,76]. The numerical minimization of the sum of the dissimilarities of the observations to their closest representative group was used as a truncation criterion to choose the optimal number of clusters [77]. The spatial localization (i.e., longitude and latitude), land cover, type of climate, and terrain elevation were considered as local factors, which have been shown to influence the spatial distribution of precipitation in Amazonia [15,53]. As mentioned in Section 2.2.4, the type of climate, land cover, and terrain elevation were obtained from auxiliary satellite-based datasets. All datasets were resampled using the nearest neighbor technique to match the 0.5-degree latitude by 0.5-degree longitude grid of the SPEI. For the sake of simplicity, the land cover was categorized into forest, grassland, cropland, and other. The type of climate was classified into Aw (tropical savannah), Af (tropical rainforest), Am (tropical monsoon), and other. The terrain elevation was categorized into four groups (i.e., low, medium, high, and very high) by a quantile classification algorithm, which distributes the elevation data into categories having an equal amount of data. Figure 2 summarizes the above analysis methods that were applied for this study.

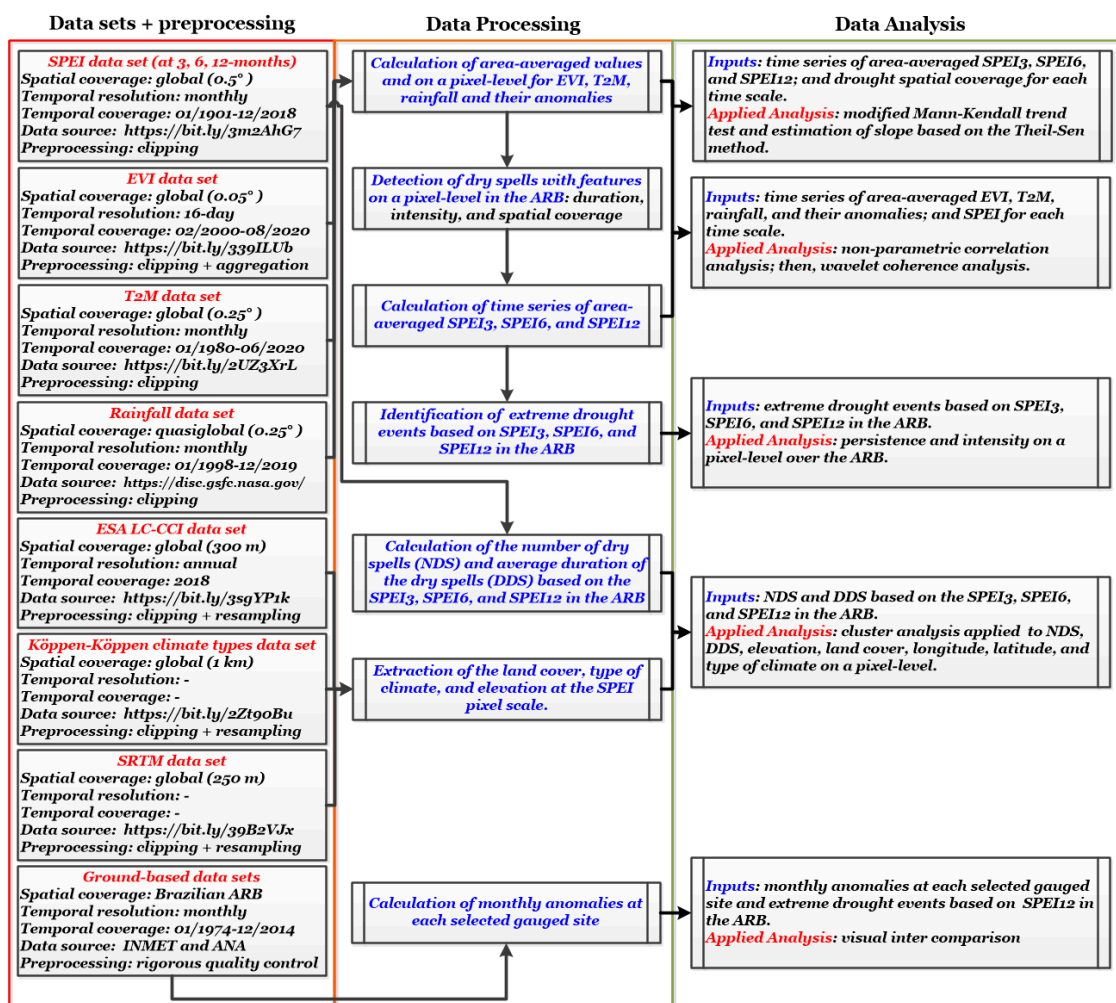
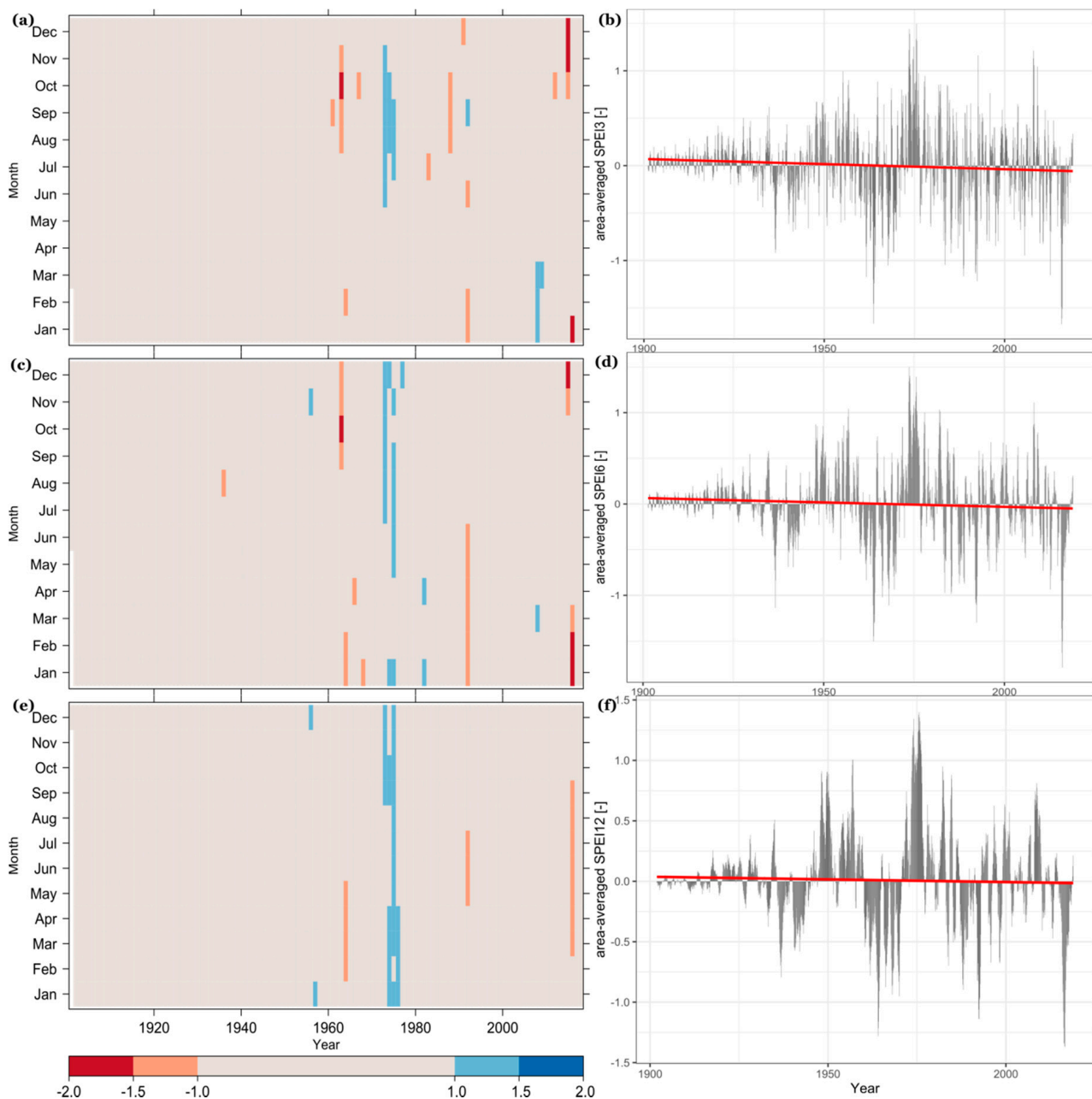


Figure 2. Simplified flowchart of the activities that were developed for this study.

### 3. Results

#### 3.1. Long-Term Temporal Patterns of Drought Events in the Entire ARB

Figure 3 shows the evolution of the values of SPEI at the 3- (SPEI3; Figure 3a,b), 6- (SPEI6; Figure 3c,d), and 12-month time scales (SPEI12; Figure 3e,f) averaged over the entire ARB during the period 1901–2018; all time series were calculated using the median to minimize the bias caused by any outlier in the data. The values greater than 1.00 shown in blue and cyan indicate the dominance of wet conditions, whereas the lower values, less than  $-1.00$ , shown in orange and red, indicate the dominance of dry conditions.



**Figure 3.** Long-term temporal variation of the area-averaged values of SPEI at a: (a,b) 3-month time scale (SPEI3); (c,d) 6-month time scale (SPEI6); and (e,f) 12-month time scale (SPEI12) in the ARB during 1901–2018. The calculation of the average is based on the median. The red line indicates the fitted line. The reference period is 1901–2018.

The area-averaged values of SPEI3 ranged from  $-1.672$  to  $1.496$  with a median equal to  $0.023$ ; the area-averaged values of SPEI6 ranged from  $-1.791$  to  $1.499$  with a median



equal to 0.016; and the area-averaged values of SPEI12 ranged from  $-1.370$  to  $1.399$  with a median equal to  $0.003$ . Regardless of the time scale used in the calculation of the SPEI, dry conditions prevailed in the years 1964, 1992, and 2016 (SPEI median:  $-0.517$ ), while wet conditions prevailed in the period 1973–1975 (SPEI median:  $0.856$ ) (see Figure 3). The monthly time series of SPEI3 and SPEI12 showed the predominance of drought conditions throughout the period of 2015–2016 (SPEI median:  $-0.612$ ). It is important to note that drought conditions were relatively frequent in the ARB, particularly since 1975 (the number of months with the area-averaged SPEI median  $\leq -1.00$  were equal to 13, 11, and 10 for the 3-, 6-, and 12-month time scales, respectively), though their intensities vary based on time scale. The more extensive drought conditions were observed in 1964, 1992, and 2016 (Figure 4), where more than 30% of the entire ARB (roughly  $1,794,693 \text{ km}^2$ ) was affected by drought conditions at all time scales during several consecutive months. These results suggest the presence of an underlying multi-decadal oscillation in the occurrence of extensive drought conditions, which may be attributed to the effects of the Pacific and Atlantic multi-decadal variability on rainfall in the ARB [78].

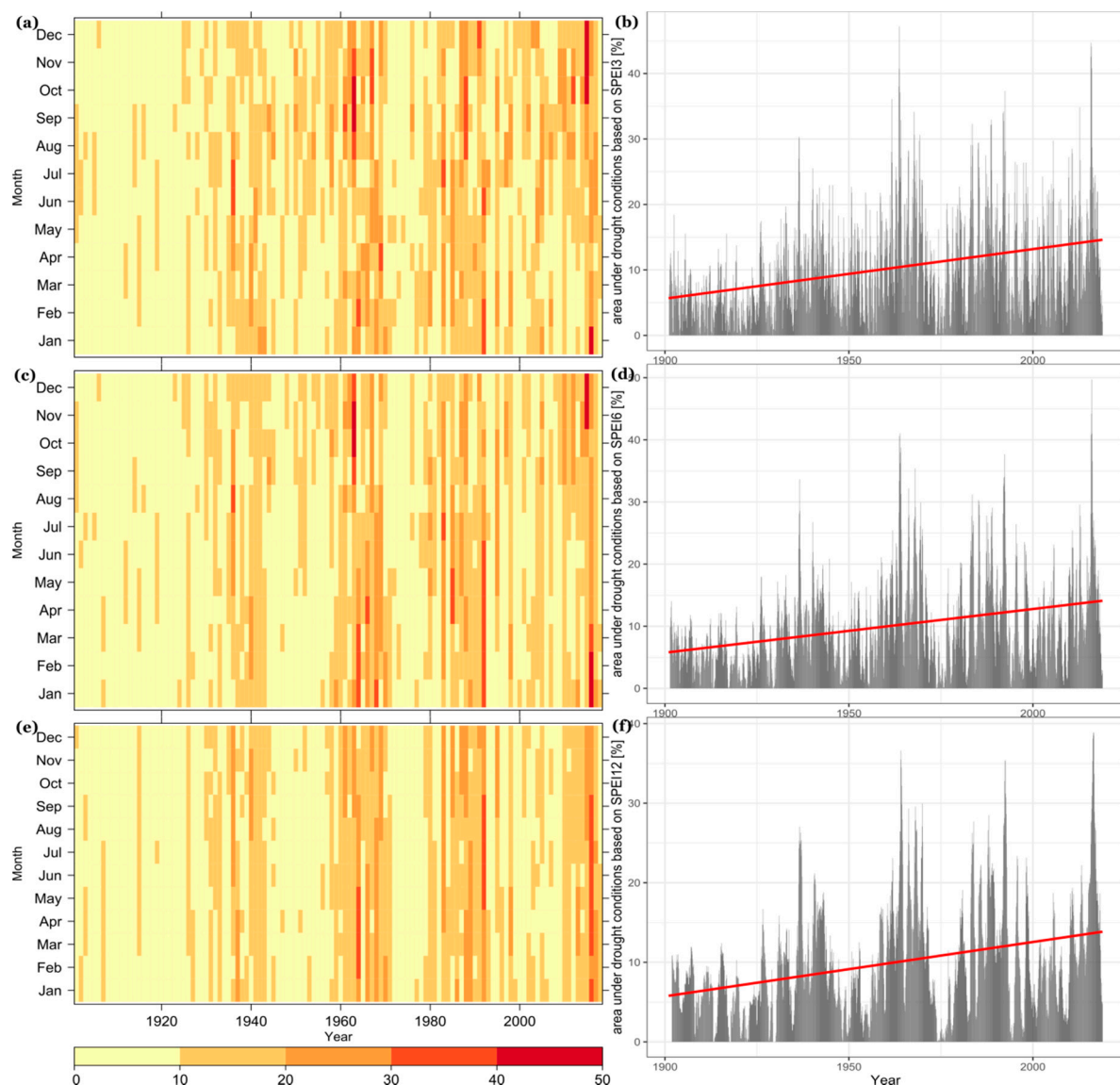


**Figure 4.** Percentage of area under drought conditions according to the values of: (a,b) SPEI3; (c,d) SPEI6; and (e,f) SPEI12 in the ARB during 1901–2018. The calculation of the drought spatial coverage is based on the number of pixels with values of SPEI  $\leq -1.00$ , regardless of the time scale used. The red line indicates fitted line. The reference period is 1901–2018.

In terms of trends observed at 5% significance level throughout the ARB from 1901 to 2018, significant decreasing trends in the time series of SPEI3 (Theil-Sen slope:  $-6.98 \times 10^{-5}$ ), SPEI6 (Theil-Sen slope:  $-6.47 \times 10^{-5}$ ), and SPEI12 (Theil-Sen slope:  $-1.32 \times 10^{-5}$ ) were observed (see Figure 3). In contrast, significant increasing trends in the time series of the percentage of area under drought conditions based on the SPEI3 (Theil-Sen slope: 0.005%), SPEI6 (Theil-Sen slope: 0.004%), and SPEI12 (Theil-Sen slope: 0.004%) were observed (see Figure 4). These results indicate the occurrence of a long-term drying trend over an increasingly larger portion of the ARB throughout the 1901–2018 time period.

In order to explore the extreme drought events in the ARB, Table 2 summarizes their main features during the analysis period. The most severe event for each time scale occurred from July 1963 to March 1964 (SPEI3), from October 2015 to September 2016 (SPEI6), and from August 2015 to August 2017 (SPEI12). This last event showed the highest severity (37.79) due to the exceptional character of its duration (21 months), although the intensity was relatively low throughout the period. From Table 2, one can see that the more severe events exhibited lower intensities than the absolute minimum value for each time scale analyzed. These findings suggest that the most severe droughts tend to be longer and with low intensity.

**Table 2.** Main features of the extreme drought events <sup>1</sup> identified over the ARB during 1901–2018.

Time Scale [Months]	Event	Start [Date]	End [Date]	Duration [Months]	Intensity [-]	Dry Area Peak [%]	Severity [-]
3	E1	April-36	August-36	5	1.76	30.34	8.81
	E2	July-63	March-64	<b>9</b>	1.77	<b>47.19</b>	<b>15.95</b>
	E3	August-67	February-68	7	1.73	34.14	12.14
	E4	February-85	July-85	6	<b>1.87</b>	29.44	11.22
	E5	August-88	December-88	5	1.80	32.95	9.01
	E6	November-91	March-92	5	1.73	34.20	8.66
	E7	August-15	March-16	8	1.78	44.71	14.25
6	E1	May-36	October-36	6	1.73	33.66	10.36
	E2	August-63	May-64	10	1.78	41.05	17.84
	E3	January-66	June-66	6	1.72	32.18	10.35
	E4	August-67	July-68	<b>12</b>	1.77	35.42	21.28
	E5	March-69	August-69	6	1.75	29.93	10.47
	E6	February-83	November-83	10	1.77	31.18	17.68
	E7	April-85	August-85	5	<b>1.88</b>	30.31	9.40
	E8	September-88	January-89	5	1.77	29.09	8.83
	E9	December-91	August-92	9	1.77	37.67	15.90
	E10	May-95	October-95	6	1.79	26.42	10.71
	E11	September-12	January-13	5	1.73	29.57	8.64
	E12	October-15	September-16	<b>12</b>	1.80	<b>49.73</b>	<b>21.58</b>
12	E1	June-36	April-37	11	1.71	27.03	18.79
	E2	September-63	September-64	13	1.82	36.61	23.64
	E3	January-66	June-66	6	1.72	29.32	10.35
	E4	November-67	August-68	10	1.77	29.57	17.73
	E5	August-69	February-70	7	1.72	29.96	12.07
	E6	April-83	December-83	9	1.79	27.68	16.1
	E7	September-85	January-86	5	<b>1.85</b>	22.27	9.24
	E8	October-87	April-88	7	1.72	28.48	12.05
	E9	September-88	July-89	11	1.74	22.44	19.14
	E10	December-91	December-92	13	1.78	35.36	23.18
	E11	August-15	August-17	<b>21</b>	1.78	<b>38.89</b>	<b>37.39</b>

<sup>1</sup> The drought spatial coverage is greater than 20% of the entire ARB during at least five consecutive months; for each feature, the extreme value is reported in bold. The severity is the absolute value of the sum of the values of SPEI from the start to end of the dry spell. The intensity is the ratio between the severity and the duration of a dry spell. The dry area peak is the maximum value of the percentage of pixels with values of  $SPEI \leq -1.00$  during the dry spell.

Another interesting aspect revealed by the SPEI time series was that the extreme drought events tended to be more frequent since 1960, in particular at the 6- and 12-month time scales (Figure 5), which is in line with the observations-based results reported by the AR5-IPCC [16] and other recent studies aimed at the analysis of droughts in the Amazonia [4,7,9,34]. It should be noted that the upward trend in extreme drought events should be interpreted with caution because the CRU TS-based SPEI dataset during the first half of the 20th century is based on a relatively low number of ground-based climatic data [58], which can generate a moderate uncertainty in relation to its capability to detect extreme drought events in the ARB before the 1960s.

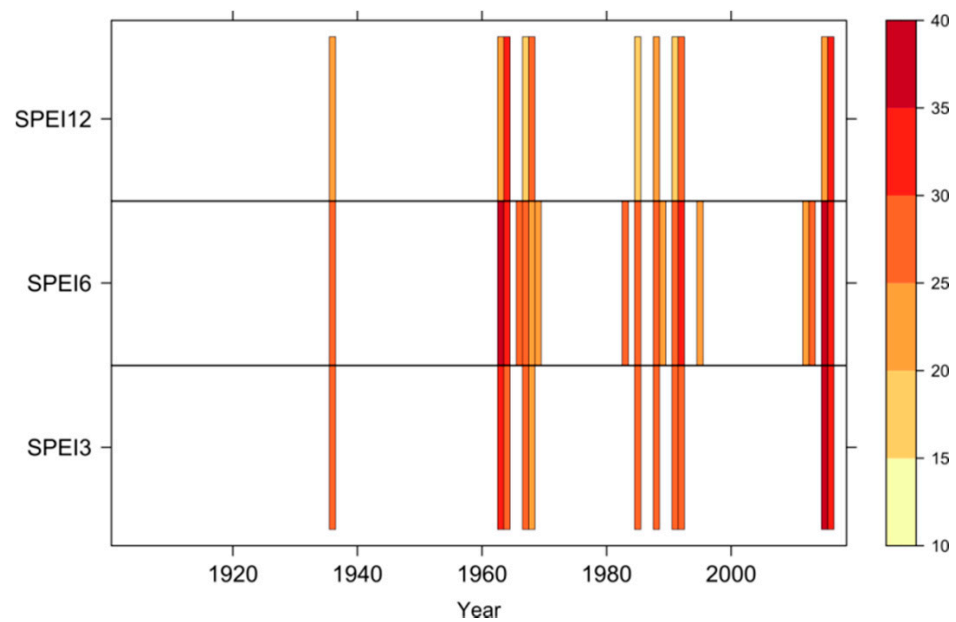


**Figure 5.** Drought spatial coverage of the extreme drought events based on the SPEI3, SPEI6, and SPEI12 time series in the ARB during 1901–2018. The calculation of the drought spatial coverage is based on the number of pixels with values of  $\text{SPEI} \leq -1.00$ , regardless of the time scale used.

To investigate the impacts of the extreme drought events in terms of intensity and temporal persistence, each extreme drought event listed in Table 2 was isolated. Then, the intensity and the temporal persistence were calculated for each pixel using the methods described earlier. Figure 6 displays the spatial distribution of the intensity and the temporal persistence over the ARB during the incidence of the SPEI3, SPEI6, and SPEI12 extreme drought events. A visual inspection of this figure reveals that the SPEI3-based E4 event showed a relatively large area with the highest values of intensity (intensity values  $>3$ ) on the low part of the Ucayali and Napo River sub-basins near the Peru–Brazil border (see Figure 6a). In contrast, the other drought events were characterized by the presence of large areas with low to moderate intensity (intensity values  $\leq 3$ ). A high temporal persistence of drought conditions was observed on large geographical regions for all drought events regardless of the local intensity (see Figure 6b).

Regarding the SPEI6-based extreme drought events, a similar pattern to the SPEI3-based extreme drought events in terms of intensity and temporal persistence was observed. That is, they tended to show a low intensity and high persistence over large areas of the ARB, except for the SPEI6-based E7 event, which was characterized by the occurrence of values of high intensity in lower portions of the Ucayali and Napo River sub-basins (Figure 6c). Similarities were also observed when the SPEI12-based extreme drought events were considered (see Figure 6e,f). Interestingly, these results are consistent with Table 2 and reveal that the impact of the extreme drought events was based primarily on their long persistence rather than their intensity.

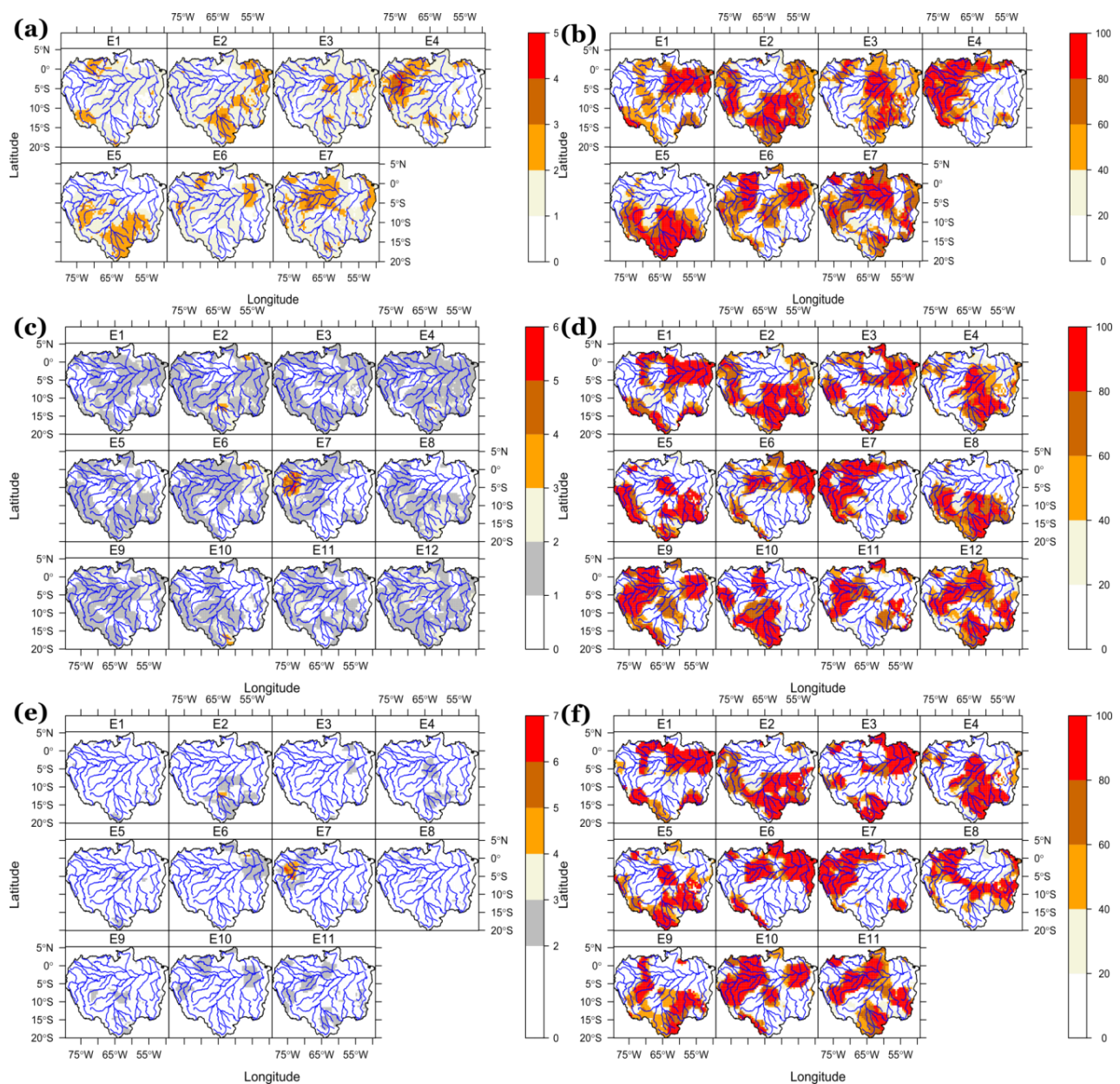


**Figure 6.** Spatial distribution of the intensity [–] and the temporal persistence [%] during the occurrence of the: (a,b) SPEI3-based extreme drought events; (c,d) SPEI6-based extreme drought events; and (e,f) SPEI12-based extreme drought events over the ARB during 1901–2018. The main features of the extreme drought events are shown in Table 2. The temporal persistence is the percentage of the total duration of the extreme drought event on a pixel-level.

A detailed comparison, considering the intensity and the temporal persistence simultaneously for the 3-, 6-, and 12-month time scales showed that the SPEI3-based E4 event and the SPEI6-based E7 and SPEI12-based E7 events were a concurrent event (see Figure 6). Note that this event affected a well-defined region on the lower part of the Ucayali and Napo River sub-basins, exhibiting a relatively low temporal persistence in relation to drought conditions on surrounding regions at the 6- and 12-month time scales. The more detailed inspection of this event in Figure 6 suggested the incidence of a dry spell with a very high intensity (the values of intensity were greater than 4.00 at the pixel level) but with a relatively short temporal evolution.

### 3.2. Land–Atmosphere Coupling during the more Recent Extreme Drought Events in the ARB

This section investigates the land–atmosphere coupling during the more recent drought events in terms of their impacts on vegetation, temperature, and streamflow. In order to select the most adequate time scale to assess the land–atmosphere coupling, the Spearman rank correlation coefficient between the paired values of SPEI at different time scales against the EVI, T2M, and rainfall (including their monthly anomalies) using a lag time of zero months during their common time periods was applied (Table 3). The Spearman rank correlation coefficient is adopted because of the predominance of a non-Gaussian distribution in these time series and their respective anomalies (not shown).

**Table 3.** Spearman rank correlation coefficients between the SPEI3, SPEI6, and SPEI12 and the EVI, T2M, and rainfall in the ARB during their common time periods <sup>1</sup>.

Auxiliary Satellite-Based Variable	Period [Years]	SPEI3 [-]	SPEI6 [-]	SPEI12 [-]
EVI [-]	2001–2018	−0.064	<b>−0.250</b> *	−0.019
EVI anomalies [-]		−0.077	−0.033	−0.120 *
T2M [°C]	1980–2018	−0.339 *	−0.354 *	−0.208 *
T2M anomalies [°C]		<b>−0.515</b> *	−0.414 *	−0.279 *
Rainfall [mm/month]	1998–2018	0.353 *	0.097	0.119 *
Rainfall anomalies [mm/month]		<b>0.559</b> *	0.379 *	0.331 *

<sup>1</sup> For each area-averaged auxiliary satellite-based variable, the Spearman correlation coefficient with the highest magnitude is reported in bold; \* statistical significance at 95% level based on an asymptotic t approximation.

The Spearman correlation coefficient (R) for the SPEI6 against the EVI (R value: −0.250) and for the SPEI3 against the anomalies of T2M (R value: −0.515) and rainfall (R value: 0.559) showed the highest magnitudes (Table 3). The T2M and rainfall were more sensitive than the EVI to short-term changes in precipitation and temperature reflected by the SPEI3. A moderate delay in the response of the vegetation to climatic conditions was also evidenced by the strength of correlation between the SPEI6 and the EVI.

In the ARB, the forest is the most prominent land cover (about 83% of its entire surface) [8]; therefore, the EVI spatiotemporal variability can be mainly attributed to seasonal changes in the vegetation greenness in the Amazon forest [79] and other edaphoclimatic factors, such as soil-moisture retention and evapotranspiration [37]. It is well-known that during the occurrence of prolonged warm and dry conditions, the vegetation phenology is mostly driven by the soil water availability and the adaptive strategy to prevent excessive water loss used by plants (e.g., the stomatal closure) [80]. These mechanisms can help to explain the above-mentioned moderate delay between the SPEI6 (the climate signal) and EVI (the vegetation signal). On the other hand, the highest association between the SPEI3 against the T2M and rainfall when the last two variables were expressed as anomalies (see Table 3) can be mainly explained by the effect of noise suppression in the native data of T2M and rainfall during the calculation of the monthly anomalies, leading to enhanced temporal coherence between both signals.

To gain further insights on the land–atmosphere coupling throughout the more recent drought events, wavelet coherence analysis (WCA) was applied considering the SPEI6 against the EVI and the SPEI3 against the anomalies of T2M (T2Ma) and rainfall (RA). For this analysis, these variables were previously area-averaged over the entire ARB. Unlike the correlation analysis, the WCA allows the calculation of the intensity of the covariance and the phase difference between the two time series in a time–frequency domain [73,81]. Squared wavelet coherence together with their phases for SPEI6–EVI, SPEI3–T2Ma, and SPEI3–RA are shown in Figure 7. In Figure 7b,d,f, the blue color indicates low wavelet coherence (near zero), whereas the red color shows areas of high wavelet coherence (near one).

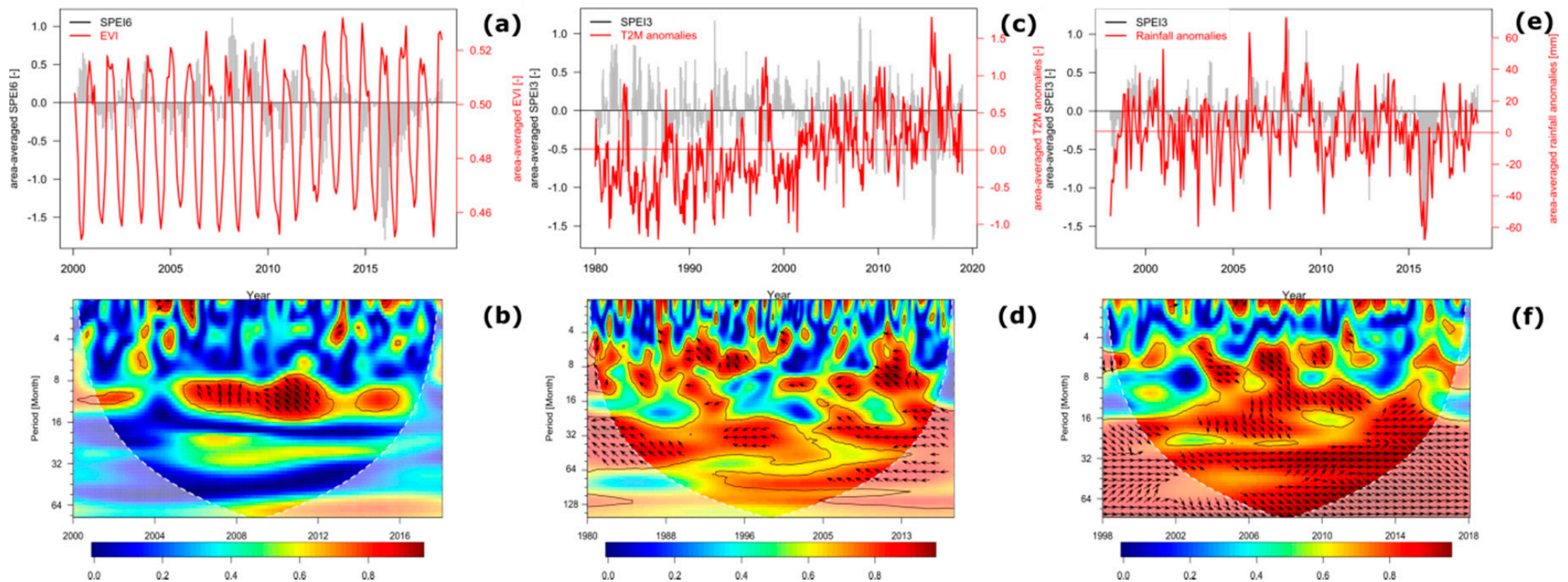


**Figure 7.** Temporal variation of the area-averaged values over the entire ARB of the: (a) SPEI6 against EVI during 2001–2018; (c) SPEI3 against T2Ma during 1980–2018; (e) SPEI3 against RA during 1998–2018 in the ARB; and the squared wavelet coherence between the times series shown in: (b) Figure 7a; (d) Figure 7c; and (f) Figure 7e. Thick contours enclose the areas with correlations statistically significant at 95% confidence level against red noise. Semitransparent areas indicate the ‘cone of influence’ where the edge effects become important; therefore, they were not analyzed [73]. The relative phase relationship is shown as arrows (with in-phase pointing right, anti-phase pointing left, SPEI6 or SPEI3 leading auxiliary variable by 90° pointing straight down, and auxiliary variable leading SPEI6 or SPEI3 by 90° pointing straight up).

An inspection of Figure 7 shows that the SPEI6 against EVI and the SPEI3 against T2Ma and RA had different degrees of coherence for a variety of periods and time scales. The wavelet coherence between the SPEI6 and EVI revealed areas with the highest common power at recurrence intervals of 9–12 months from 2009 to 2012 (significant at 95% level), in which the EVI signal tended to lead the SPEI6 signal, indicating that there was an asynchronous coupling in intensity and direction of the correlation between the SPEI6 and EVI during this period. It should, however, be noted that the SPEI6-based E11 and E12 extreme drought events (see Table 2; from September 2012 to January 2013 and from October 2015 to September 2016, respectively), coincided with an abrupt coupling between the signals of SPEI and EVI with recurrence times of 1–4 months (i.e., arrows in-phase in Figure 7b). As noted by Zhao et al. [82], the forest and other land cover types (e.g., grassland and non-irrigated) tended to show low physiological resistance to very persistent water deficits in the ARB.

The wavelet coherence between the SPEI3 and T2Ma exposed large areas with high significant power at recurrence intervals of 25–40 months from 1980 to 2018, in which the signals of SPEI3 and T2Ma tended to be in anti-phase, indicating that there was a synchronous coupling in intensity but with inverse direction in the relationship between the SPEI3 and T2Ma for this period. It is also important to mention that during the occurrence of the SPEI3-based extreme drought, events E4 (from 02/1985 to 07/1985), E5 (from 08/1988 to 12/1988), and E6 (from 11/1991 to 03/1992) were observed in small areas with high significant power at recurrence intervals of 4–8 months, indicated that these events were characterized by the concurrent combination of drought conditions and heat waves (see Figure 7c). Another aspect evident in Figure 7c is a temporal tendency towards warmer-than-normal conditions since the beginning of 2000, which reached an exceptional peak during the evolution of the SPEI3-based E7 extreme drought event (from 08/2015 to 03/2016), after which a bounce-back effect was observed (September 2015).

The wavelet coherence between the SPEI3 and RA was relatively comparable to that obtained for the SPEI3 against T2Ma (see Figure 7d,f), even though the SPEI3-RA showed high significant power during most parts of the period analyzed (i.e., 1988–2018). As expected, Figure 7f reveals a significant power at recurrence intervals of 30–64 months from 1988 to 2018 where both signals are in phase, meaning that the rainfall variability has a strong contribution to the occurrence of drought conditions in the ARB, particularly when persistent drought conditions were observed (e.g., during the occurrence of the SPEI3-based E7 extreme drought event between August 2015 and March 2016). Unlike the T2Ma, the RA did not experience a clear tendency towards drier-than-normal conditions in terms of the amount of precipitation received over the ARB (see Figure 7c,e).

In order to investigate the impacts of drought conditions on streamflow, a visual inspection of the streamflow and rainfall anomalies on a monthly time scale at certain rivers was conducted to examine their response to drought conditions during the period 1974–2013. The major rivers Amazon, Curua, Jari, Madeira, Maicuru, Macajai, Purus, and Xingu were considered for this analysis (see Figure 1c). The rationale behind the choice of this period is that the ground-based data from the ANA and INMET contain few gaps (less than 10% missing data per month). The SPEI12-based extreme drought events were chosen because this time scale has been widely used for assessing hydrological droughts [21,83]. Figure 8(a1–a13) display the streamflow anomalies, while Figure 8(b1–b5) depict the rainfall anomalies. Furthermore, Figure 8c–g show the spatial distribution of the temporal persistence of drought conditions for the extreme drought events E6, E7, E8, E9, and E10 based on the time scale of 12 months (see Figure 6e,f)

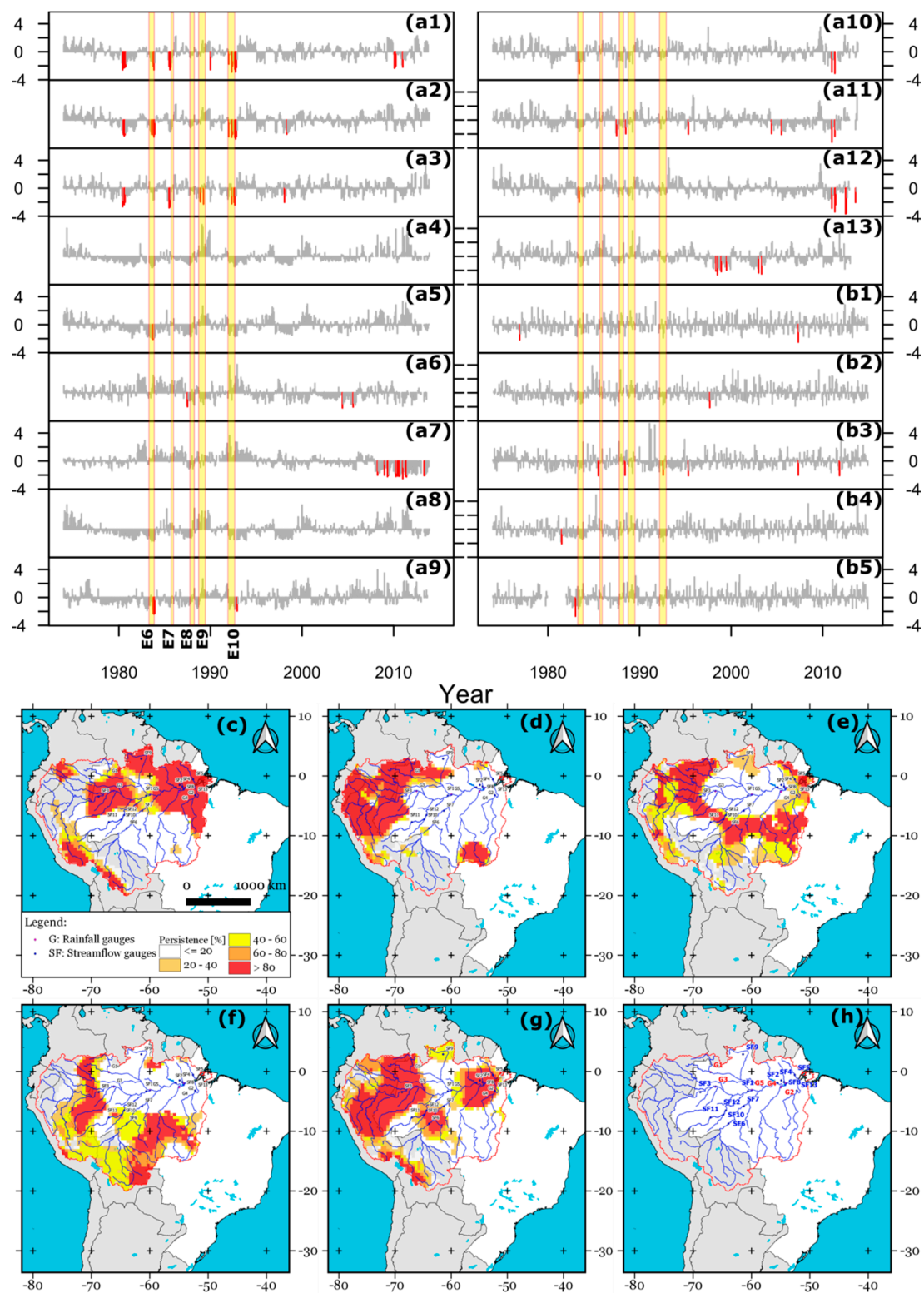


**Figure 8.** The monthly streamflow anomalies [ $\text{m}^3/\text{s}$ ] at the streamflow gauges shown in (h) as: SF1 (a1), SF2 (a2), SF3 (a3), SF4 (a4), SF5 (a5), SF6 (a6), SF7 (a7), SF8 (a8), SF9 (a9), SF10 (a10), SF11 (a11), SF12 (a12), and SF13 (a13). The monthly rainfall anomalies [mm/month] at the rainfall gauges shown in (h) as: G1 (b1), G2 (b2), G3 (b3), G4 (b4), and G5 (b5). The temporal persistence of drought conditions [%] during the occurrence of the SPEI12-based extreme drought events: E6 (c), E7 (d), E8 (e), E9 (f), and E10 (g). The spatial distribution of the streamflow [blue] and rainfall [red] gauges is shown in (h). The month of start and end for each event is shown in panels (a1) to (b5). The negative anomalies less than -2 in panels (a1) to (b5) are shown with red bars. Base period for the calculation of anomalies: 1974–2013.



Despite the low density of the hydrometeorological network and the poor distribution of the gauges within the ARB (see Figure 8h), the SPEI12-based climate response showed good agreement with the in-situ data in those sub-basins affected by drought conditions during the occurrence of the SPEI12-based events (see Figure 8(a1–a13)), implying that the SPEI12 captured the spatial distribution of the long-term droughts reasonably well in the ARB, as well as its temporal behavior. A more detailed examination of the streamflow gauges with negative anomalies revealed that the upstream areas of their catchments were totally or partially affected by drought conditions. This distinctive feature, which was particularly evident through the E6 event, implied that the evolution and propagation of one meteorological drought event into one hydrological drought event was heavily dependent on the spatial coverage and persistence of drought conditions within the sub-basins upstream of the streamflow gauge in addition to the catchment characteristics [84]. Note that the E6 event was concentrated mostly over the northern and northeastern parts of the ARB (Figure 8c) and was also concurrent with strong anomalies at almost all streamflow gauges (excepting the Madeira River, see Figure 1c). Nevertheless, as shown in Figure 8(a1–a13), the occurrence of negative streamflow anomalies was not necessarily indicative of the existence of an extreme drought event. For instance, a dry spell spatially concentrated over a part or the entirety of one sub-basin can lead to local hydrological drought (e.g., see the red bars in Figure 8(a7)).

### 3.3. The Regions of the ARB more Prone to Suffering Drought Events

The previous analyses provided limited information on the drought episodes that were not classified as extreme drought events (i.e., dry area:  $\geq 20\%$  of the ARB and duration:  $\geq 5$  months). However, as can be seen from Figure 8(a1–b5), there was a pronounced occurrence of dry episodes with drought coverage less than 20% in the ARB (henceforth dry spells), particularly since 1975. This limitation was overcome by calculating the frequency of dry spells and their duration within each pixel of the SPEI3, SPEI6, and SPEI12 for the period 1975–2018. For consistency, those events with a duration less than 2 months were not considered as dry spells. The spatial distribution of the number of dry spells is shown in Figure 9a, while Figure 9b displays their average duration.

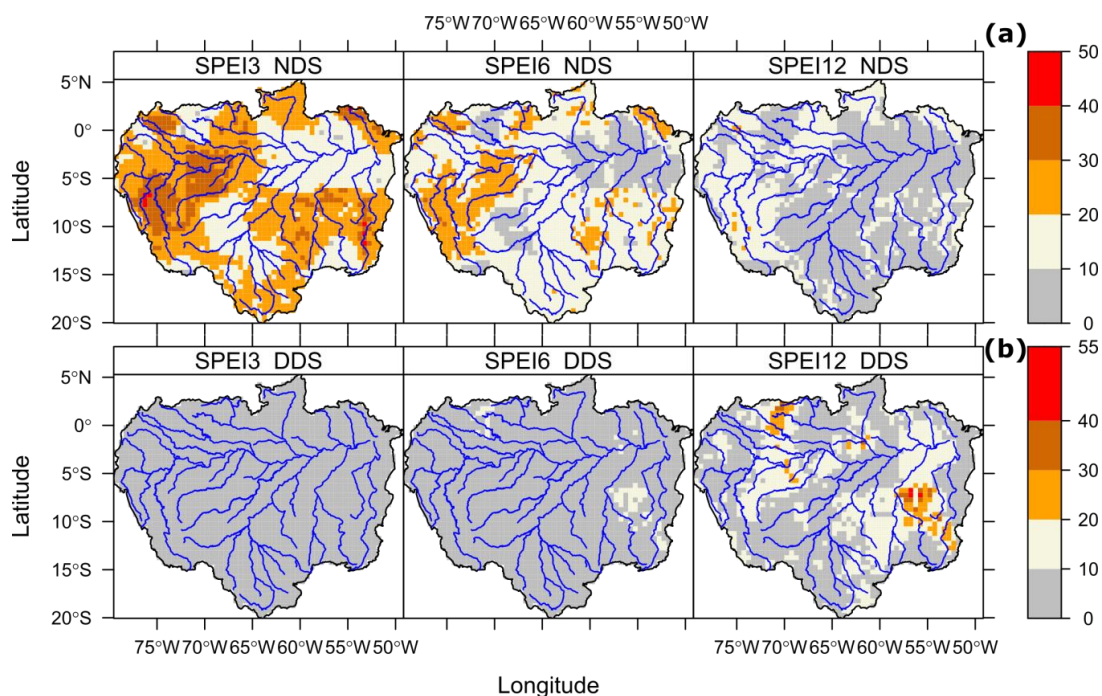


**Figure 9.** The spatial distribution during 1975–2018 of (a) the number of dry spells [NDS] based on the SPEI3, SPEI6, and SPEI12, respectively; (b) the average duration of the dry spells [DDS] based on the SPEI3, SPEI6, and SPEI12, respectively. The average duration of the dry spells is shown in months.

The number of dry spells [NDS] tended to be shorter when the SPEI time scale increased (Figure 9a). In contrast, the average duration of the dry spells [DDS] tended to be longer when the SPEI time scale increased (Figure 9b). A few studies have suggested that the impacts of drought events in some regions of the ARB are associated with the precipitation variability [48] and other local factors such as topography [85], vegetation [82], and dominant climate conditions [50]. For this reason, a medoids-based cluster analysis was used to explore the association between both the NDS and DDS with the terrain elevation, land cover, and type of climate based on the Köppen-Geiger climate classification in the ARB. According to this analysis, there are two subregions in the ARB with marked differences in terms of NDS and DDS. Figure 10a shows the spatial distribution of these subregions, while the land cover, terrain elevation, and type of climate are shown in Figure 10b–d. As can be seen, the C2 region is characterized by the occurrence of the most extreme dry spells in terms of NDS (median NDS: 27, 19, and 11 dry spells for time scales of 3, 6, and 12 months) and DDS (median DDS: 3.71, 5.56, and 9.27 months for time scales of 3, 6, and 12 months). On the other hand, the C1 region showed median values of 16, 11, and 6 dry spells for NDS, and 3.39, 5.00, and 9.00 months for DDS at time scales of 3, 6, and 12 months, respectively. This reveals the presence of a well-defined region where the frequency of dry spells was much higher than that in other regions of the ARB (Figure 10a), even though their duration tended to be similar (see DDS in Figure 9).

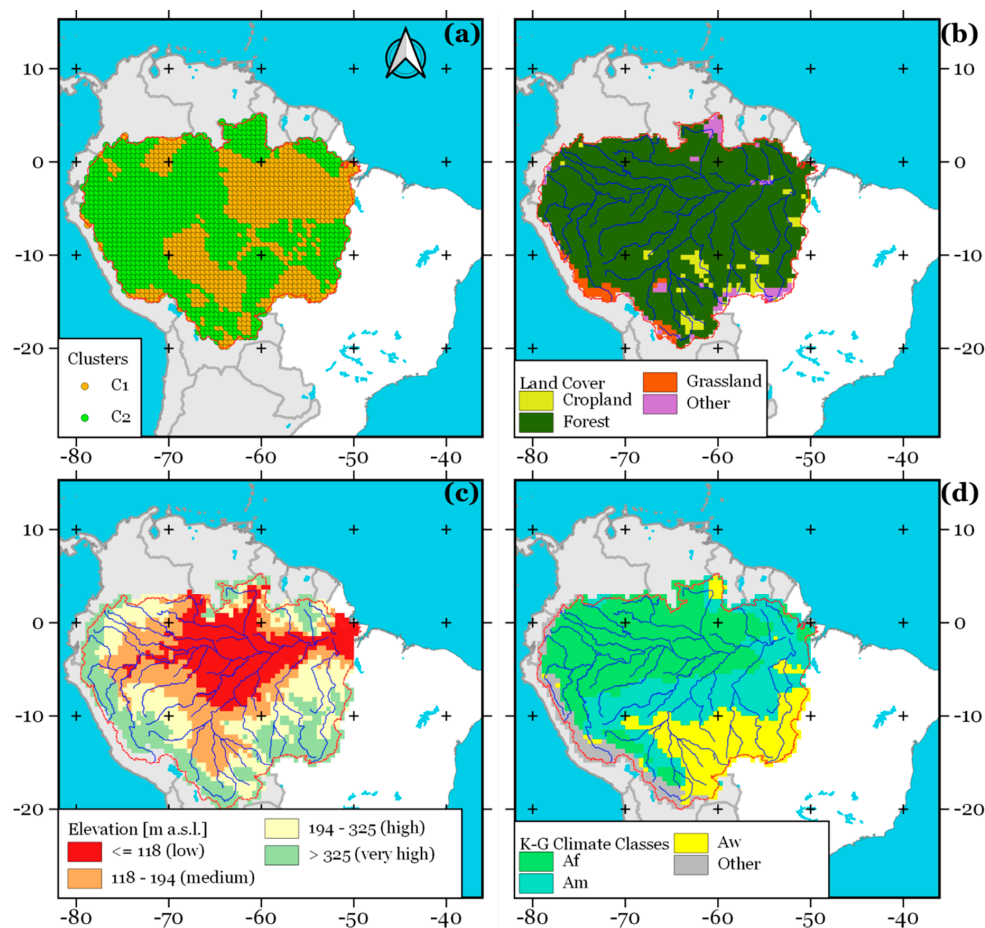


**Figure 10.** The spatial distribution of (a) the SPEI pixels according to results from cluster analysis applied to the number of dry spells [NDS], average duration of the dry spells [DDS], spatial localization of SPEI pixels, land cover, type of climate, and terrain elevation; (b) the land cover type; (c) the terrain elevation in m a.s.l.; and (d) the type of climate based on the Köppen-Geiger climate classification [46]. NDS and DDS are based on the time series of SPEI3, SPEI6, and SPEI12 for the period 1975–2018. The spatial localization refers to longitude and latitude in degrees for each SPEI pixel. The land cover map that is referred to is from 2018.

When the local factors are analyzed in terms of NDS for the C2 region, the results reveal that the variation range of NDS for the land cover is slightly higher than that for the terrain elevation and the type of climate (not shown). Nevertheless, this finding is not necessarily indicative of the forest being more sensitive to drought than other land cover classes. The fact that forests is the predominant land cover (about 92% of the total area in the ARB) can help to explain this slight difference in NDS values between land cover classes. In other words, there is no clear evidence that the high incidence of drought in different regions of the ARB (C2 in Figure 10a) is associated to terrain characteristics, land cover, and type of climate.

Overall, the results indicated that the greater part of the sub-basins Ucayali, Japurá-Caquetá, Jari, Jutai, Marañón, Tapajós, and Xingu (see Figures 1c and 10a) exhibited a high incidence of dry spells (NDS > 20 events) with short durations (DDS ≤ 10 months). Therefore, these regions were especially prone to both short-term droughts (Figure 9) and extreme drought events (Figure 6). On the other hand, the remarkable regional persistence of long-term drought conditions on the sub-basins Tapajós and Xingu (Figure 9b for SPEI12) was a relevant finding due to the potential impacts of drought on two key sectors: rainfed agricultural and hydropower production.

#### 4. Discussion

In short, there were strong drought conditions in 1964, 1992, and 2016, while wet conditions were dominant from 1973 to 1975 (see Figure 3). The basin-wide extreme dryness coincided with high SST anomalies over the Tropical North Atlantic (TNA) region in 1964 [86], but it was concurrent with strong El Niño episodes in 1992 and 2016 [87]. These years were also characterized by deficits of precipitation across more than 30% of the basin through various successive months (see Figure 4). In contrast, unusually cool surface waters concentrated in the central Pacific (La Niña) between 1973 and 1975 coincided with prolonged rainfall events in the greater part of the ARB [88]. Several previous studies have showed the modulation of the precipitation on vast regions of the ARB by the SST variability in the TNA and Tropical Pacific regions among other large-scale ocean-atmosphere teleconnections [4,8,34,48]. While intraseasonal precipitation variability is mainly driven by the Madden–Julian Oscillation (MJO) [89], the combined influence of the Pacific Decadal Oscillation (PDO) and the Atlantic Multidecadal Oscillation (AMO) can modulate the effects of ENSO on the spatiotemporal distribution of precipitation across the basin at larger scales [20,48]. Even though other climate modes of natural variability have been identified, the ENSO, MJO, PDO, AMO, and their interactions play an important role on hydroclimatic regime in the ARB [6,90], particularly when they act in synergy blocking the moisture transport from the TNA to the basin [4,78]. Therefore, the basin-wide drought conditions on the ARB may be partially attributed to the influence of the dominant climate modes and their interactions on all time scales. Nevertheless, it should be emphasized that numerous studies using remote sensing techniques have demonstrated that their impacts can be exacerbated by anthropogenic factors (e.g., expansion of agricultural lands) [13,91].

Although results showed the presence of a weak long-term drying trend together with basin-wide drought conditions at the 3-, 6-, and 12-month time scales (see Figures 3 and 4), there was no clear evidence of a trend in the extreme drought events in terms of their spatial coverage, intensity or duration during the entire study period 1901–2018 (see Table 3), which is consistent with the findings of previous studies [92,93]. Nonetheless, the basin-wide drought conditions have become more frequent since the 1970s when compared to other decades (see Figure 5), suggesting a progressive transition to drier-than-normal conditions (see Figure 7). This result is in agreement with a few studies that pointed out the presence of underlying decadal and multi-decadal cycles in the hydrological regime of the ARB [43], which, in turn, are related to the main modes of variability such the PDO and the AMO [20]. The transition from wetter-than-normal conditions to drier-than-normal conditions (see Figure 7c,e) was concurrent with a shift of the AMO signal registered around 2000 (from cold to warm) [94], which, in turn, was frequently coupled with the PDO signal,

and thus, with the occurrence of stronger El Niño events [90,95,96]. The concurrence of these climate modes of natural variability may explain part of the intensification of drought conditions, heat waves, and extensive fires in recent decades over the ARB [9].

The drought events that were spatially more extensive and temporally persistent tended to show lower intensities than those observed in other years (see Table 2). Overall, the more severe episodes were characterized by a moderate spatial concentration (see Figures 8 and 9), indicating that the impact of the basin-wide drought conditions was caused by their temporal persistence instead of the prevalence of an extreme climate dryness (i.e., severity). This distinctive behavior was evident in the lower part of the Ucayali and Napo River sub-basins (see Figures 6 and 9). As shown in Figures 3 and 4 and Table 2, the long persistence of basin-wide drought conditions was reflected by the occurrence of longer dry seasons or an excessive delay of the onset of the rainy season [87].

Another key aspect observed in the ARB was the coupling between the drought conditions and the vegetation greenness during the occurrence of basin-wide drought conditions. As expected, the vegetation greenness (dominated by forest) exhibited a strong seasonal variability (see Figure 7a), even though it was characterized by an asynchronous connection with the atmospheric dryness (see Figure 7b). This response may be explained by the combined action of the soil water storage and the adaptive strategy to prevent excessive water loss used by plants (e.g., stomatal regulation), which delay the water loss through evapotranspiration [13,57,82]. Nevertheless, this effect temporally disappeared under prolonged warm and dry conditions (see Figure 7b), meaning that the resilience of vegetation to drought reached an irreversible physiological limit [26], confirmed by the transitory coupling between the EVI and SPEI6 signals (see the lowest periods in Figure 7b). Unlike vegetation, air temperature and precipitation showed a remarkable sensitivity to dry spells, which was reflected by a rapid response to changes in short-term drought conditions (see Figure 7c,e). This situation would exacerbate the climate dryness, favoring the generation of dry biomass from different vegetation types, such as forest, grassland, shrubland, and rainfed crop, among others [34], and increasing the risk of widespread forest fires [97]; this would partially explain the high incidence of forest fires in recent years [98].

Regarding the impacts of drought conditions on streamflow, the results revealed that the severity and duration of the hydrological drought events were strongly dependent on the spatial coverage of drought conditions, their temporal persistence, and catchment characteristics within the sub-basins upstream of the river (see Figure 8). As mentioned above, the soil water holding capacity and the vegetation resiliency to drought contributed to regulate the evolution of meteorological droughts into hydrological droughts and their future evolution over time in different rivers (see Figures 7b and 8). The most intense hydrological drought episodes were not concomitant with extensive and persistent drought conditions, but were consistent with non-extensive drought events (see Figures 8 and 9). Interestingly, most of these drought events were concurrent with El Niño events, warm TNA episodes, or an overlap among them. For instance, a strong El Niño event together with warm TNA occurred during the 2010 drought, leading to wet conditions over northern Amazonia and dry conditions over southern Amazonia [8]. This fact was evident in the streamflow negative anomalies time series at the Madeira river (see Figure 8(a7)), and was also coherent with high levels of exposure to dry conditions observed in recent years over the ARB, particularly to short-term drought events (see Figure 9).

A result of particular concern was related to high recurrence of short-term drought events on the sub-basins Ucayali, Japurá-Caquetá, Jari, Jutai, Marañón, and Xingu (see Figure 1c, Figure 8a, and Figure 10a) and their relatively high level of exposure to long-term drought conditions (see Figure 6). This finding agrees with a recent work using streamflow data in Amazonia [99], confirming the presence of a drying trend over these sub-basins. Interestingly, the terrain characteristics, land cover, and the type of climate showed a very weak relationship with this drying trend (see Figure 10). The cause of this phenomenon was not elucidated from the current results because of insufficient in situ climate data. Although attribution could be made to the modes of natural variability acting

in the ARB [78], this needs further investigation, as it goes beyond the goal of this study. Regardless of its origin, these changes over these specific geographic areas have important implications on different Brazilian sectors, such as rainfed agricultural and hydropower production. In this context, one can infer that the hydrological droughts during the gradual transition to drier-than-normal conditions will tend to reduce the levels of reservoirs affecting the hydropower production, particularly over the Xingu sub-basin. Furthermore, an increased risk of food insecurity, environmental degradation, and forest fire, among other potential impacts related to extreme drought episodes, would be expected, which is in line with projected changes by some regional climate models for several regions of the ARB through the 2010–2100 period [18]. Consequently, the design and implementation of effective adaptation strategies will be necessary in the face of future droughts, implying the integration of the institutions, international non-governmental organizations, and agencies with drought management responsibilities in the ARB.

## 5. Conclusions

Several statistical approaches were used to better understand how climate variability could be affecting the spatiotemporal distribution of extreme droughts and dry spells in the ARB. The newest gridded global SPEI drought product based on the CRU TS dataset was used as a drought index at different scales (3-, 6-, and 12 months) during the period 1901–2018. The SPEI was selected due to its suitability for the analysis risk and impact assessment of meteorological, agricultural, and hydrological droughts. The following conclusions can be drawn from this study:

- Strong drought conditions in 1964, 1992, and 2016, and wet conditions from 1973 to 1975 were observed, coinciding with different patterns of coupling between the ENSO and the PDO, AMO, and MJO.
- A weak long-term drying trend was observed, but there was no evidence of a trend in extreme drought events in terms of spatial coverage, intensity, and duration for the period 1901–2018. A progressive transition from wetter-than-normal conditions to drier-than-normal conditions was evident since the 1970s, which was clearly reflected by a strong coupling between the air temperature anomalies and the drought conditions.
- The more spatially extensive and temporally persistent drought events tended to show lower intensities than those observed in other years, whereas more severe droughts were characterized by a moderate spatial concentration.
- The vegetation greenness (dominated by forest) exhibited an asynchronous connection with the atmospheric dryness, though both tend to be nearly in phase under prolonged warm and dry conditions.
- A high recurrence of short-term and long-term drought events were observed on the sub-basins Ucayali, Japurá-Caquetá, Jari, Jutai, Maraón, and Xingu of the ARB in recent years, which have important implications on key economic sectors, such as rainfed agricultural and hydropower production.

Overall, this paper has shown that basin-wide drought conditions have been worsening over the ARB in terms of spatial coverage and intensity, which was particularly evident on shorter time scales. The progressive transition from wetter-than-normal conditions to drier-than-normal conditions since the 1970s suggested a causality between the intensification of drought conditions and the incidence of the major large-scale climate variability drivers acting over the basin (e.g., AMO, PDO, and MJO). The drought conditions tended to be exacerbated by anthropogenic factors (e.g., deforestation activities) due to their negative impacts over the resilience of the forest and other land cover types in the basin. Moreover, results evidenced that the vegetation-soil feedback processes can act as a buffer factor under prolonged warm and dry conditions, delaying the propagation of meteorological droughts into hydrological drought events. However, the root cause of why certain regions of the ARB (e.g., the sub-basin Ucayali, Japurá-Caquetá, Jari, Jutai, Maraón, and Xingu) have become drought-prone areas in recent decades is still challenging. Therefore, this aspect

will be explored in future work to improve our knowledge about how climate variability is affecting the distribution of extreme droughts in the ARB.

**Supplementary Materials:** The following are freely available online at <https://zenodo.org/record/4290294>, SPEI3: SPEI3 files in GeoTiff format over the Amazon River Basin, SPEI6: SPEI6 files in GeoTiff format over the Amazon River Basin, SPEI12: SPEI12 files in GeoTiff format over the Amazon River Basin.

**Author Contributions:** F.P.-T., H.A.B., and J.G. conceived and designed the experiments; T.V.L.K. performed the experiments; M.K.T. and C.d.O.B. analyzed the data and contributed to the analysis tools. F.P.-T., H.A.B., and J.G. wrote the paper, but all authors discussed the results, and enhanced the final draft of the manuscript. All authors have read and agreed to the published version of the manuscript.

**Funding:** This work was supported by the Coordenação de Aperfeiçoamento de Pessoal de Nível Superior (CAPES 12/2020), Brazil, through Epidemias—Telemedicina e Análise de Dados Médicos, under the Grant/Award Number (23038.013745/2020-69 to H.A.B.).

**Institutional Review Board Statement:** Not applicable.

**Informed Consent Statement:** Not applicable.

**Data Availability Statement:** Not applicable.

**Acknowledgments:** This study was undertaken as part of the Epidemias project supported by the CAPES Grant. F.P.T. and C.O.B. acknowledge the support of CAPES, Brazil (Postdoctoral Grant 23038.013745/2020-69 to H.A.B.). We would like to thank: (a) the Brazilian Water Agency (ANA) and the National Institute of Meteorology (INMET) for providing climate and hydrological data; (b) the Spanish National Research Council for providing the SPEI data (<https://spei.csic.es/database.html>); (c) the NASA Land Processes Distributed Active Archive Center (LP DAAC) for providing the EVI data (<https://lpdaac.usgs.gov>); (d) the European Centre for Medium-Range Weather Forecasts (ERA5) for providing near-surface air temperature data; (e) the Goddard Earth Sciences Data and Information Services Center (GET DISC) for providing the TRMM-based rainfall data through the web-based Geospatial Interactive Online Visualization and Analysis Infrastructure (<https://giovanni.gsfc.nasa.gov>). The manuscript was improved by the insightful comments of two anonymous reviewers.

**Conflicts of Interest:** The authors declare that they have no conflict of interest.

## References

1. da Paca, V.H.M.; Espinoza-Dávalos, G.; Moreira, D.; Comair, G. Variability of Trends in Precipitation across the Amazon River Basin Determined from the CHIRPS Precipitation Product and from Station Records. *Water* **2020**, *12*, 1244. [[CrossRef](#)]
2. Michot, V.; Vila, D.; Arvor, D.; Corpetti, T.; Ronchail, J.; Funatsu, B.; Dubreuil, V. Performance of TRMM TMPA 3B42 V7 in Replicating Daily Rainfall and Regional Rainfall Regimes in the Amazon Basin (1998–2013). *Remote Sens.* **2018**, *10*, 1879. [[CrossRef](#)]
3. Sun, R.; Yao, P.; Wang, W.; Yue, B.; Liu, G. Assessment of Wetland Ecosystem Health in the Yangtze and Amazon River Basins. *ISPRS Int. J. Geo Inf.* **2017**, *6*, 81. [[CrossRef](#)]
4. Marengo, J.A.; Espinoza, J.C. Extreme seasonal droughts and floods in Amazonia: Causes, trends and impacts. *Int. J. Climatol.* **2016**, *36*, 1033–1050. [[CrossRef](#)]
5. de Albuquerque Cavalcanti, I.F.; Marengo, J.A.; Alves, L.M.; Costa, D.F. On the opposite relation between extreme precipitation over west Amazon and southeastern Brazil: Observations and model simulations. *Int. J. Climatol.* **2017**, *37*, 3606–3618. [[CrossRef](#)]
6. Giovannetone, J.; Paredes-Trejo, F.; Barbosa, H.; Santos, C.A.C.; Kumar, T.V.L. Characterization of links between hydro-climate indices and long-term precipitation in Brazil using correlation analysis. *Int. J. Climatol.* **2020**, *40*, 5527–5541. [[CrossRef](#)]
7. Marengo, J.A.; Nobre, C.A.; Tomasella, J.; Oyama, M.D.; Sampaio de Oliveira, G.; de Oliveira, R.; Camargo, H.; Alves, L.M.; Brown, I.F. The Drought of Amazonia in 2005. *J. Clim.* **2008**, *21*, 495–516. [[CrossRef](#)]
8. Jimenez, J.C.; Marengo, J.A.; Alves, L.M.; Sulca, J.C.; Takahashi, K.; Ferrett, S.; Collins, M. The role of ENSO flavours and TNA on recent droughts over Amazon forests and the Northeast Brazil region. *Int. J. Climatol.* **2019**. [[CrossRef](#)]
9. Jiménez-Muñoz, J.C.; Mattar, C.; Barichivich, J.; Santamaría-Artigas, A.; Takahashi, K.; Malhi, Y.; Sobrino, J.A.; Van Der Schrier, G. Record-breaking warming and extreme drought in the Amazon rainforest during the course of El Niño 2015–2016. *Sci. Rep.* **2016**, *6*, 33130. [[CrossRef](#)]
10. Nobre, C.A.; Marengo, J.A.; Soares, W.R. *Climate Change Risks in Brazil*; Nobre, C.A., Marengo, J.A., Soares, W.R., Eds.; Springer International Publishing: Cham, Germany, 2019; ISBN 978-3-319-92880-7.

11. Panisset, J.S.; Libonati, R.; Gouveia, C.M.P.; Machado-Silva, F.; França, D.A.; França, J.R.A.; Peres, L.F. Contrasting patterns of the extreme drought episodes of 2005, 2010 and 2015 in the Amazon Basin. *Int. J. Climatol.* **2018**, *38*, 1096–1104. [[CrossRef](#)]
12. Rao, V.B.; Franchito, S.H.; Santo, C.M.E.; Gan, M.A. An update on the rainfall characteristics of Brazil: Seasonal variations and trends in 1979–2011. *Int. J. Climatol.* **2016**, *36*, 291–302. [[CrossRef](#)]
13. Barbosa, H.A.; Lakshmi Kumar, T.V.; Silva, L.R.M. Recent trends in vegetation dynamics in the South America and their relationship to rainfall. *Nat. Hazards* **2015**, *77*, 883–899. [[CrossRef](#)]
14. Wang, X.; Yang, T.; Wortmann, M.; Shi, P.; Hattermann, F.; Lobanova, A.; Aich, V. Analysis of multi-dimensional hydrological alterations under climate change for four major river basins in different climate zones. *Clim. Chang.* **2017**, *141*, 483–498. [[CrossRef](#)]
15. Nobre, C.A.; Marengo, J.A.; Artaxo, P. Understanding the climate of Amazonia: Progress from LBA. In *Amazonia and Global Change*; Keller, M., Bustamante, M., Gash, J., Dias, P.S., Eds.; Geophysical Monograph Series; AGU: Washington, DC, USA, 2009; Volume 186, pp. 145–147.
16. Pachauri, R.K.; Allen, M.R.; Barros, V.R.; Broome, J.; Cramer, W.; Christ, R.; Church, J.A.; Clarke, L.; Dahe, Q.; Dasgupta, P.; et al. *Climate Change 2014: Synthesis Report. Contribution of Working Groups I, II and III to the Fifth Assessment Report of the Intergovernmental Panel on Climate Change*; Pachauri, R.K., Meyer, L., Eds.; IPCC: Geneva, Switzerland, 2014; ISBN 9789291691432.
17. Wang, G. Agricultural drought in a future climate: Results from 15 global climate models participating in the IPCC 4th assessment. *Clim. Dyn.* **2005**, *25*, 739–753. [[CrossRef](#)]
18. Marengo, J.A.; Chou, S.C.; Kay, G.; Alves, L.M.; Pesquero, J.F.; Soares, W.R.; Santos, D.C.; Lyra, A.A.; Sueiro, G.; Betts, R.; et al. Development of regional future climate change scenarios in South America using the Eta CPTEC/HadCM3 climate change projections: Climatology and regional analyses for the Amazon, São Francisco and the Paraná River basins. *Clim. Dyn.* **2012**, *38*, 1829–1848. [[CrossRef](#)]
19. Alves, L.M.; Chadwick, R.; Moise, A.; Brown, J.; Marengo, J.A. Assessment of rainfall variability and future change in Brazil across multiple timescales. *Int. J. Climatol.* **2020**, *41*, E1875–E1888. [[CrossRef](#)]
20. Marengo, J.A.; Borma, L.S.; Rodriguez, D.A.; Pinho, P.; Soares, W.R.; Alves, L.M. Recent Extremes of Drought and Flooding in Amazonia: Vulnerabilities and Human Adaptation. *Am. J. Clim. Chang.* **2013**, *2*, 87–96. [[CrossRef](#)]
21. Zargar, A.; Sadiq, R.; Naser, B.; Khan, F.I. A review of drought indices. *Environ. Rev.* **2011**, *19*, 333–349. [[CrossRef](#)]
22. Beguería, S.; Vicente-Serrano, S.M.; Reig, F.; Latorre, B. Standardized precipitation evapotranspiration index (SPEI) revisited: Parameter fitting, evapotranspiration models, tools, datasets and drought monitoring. *Int. J. Climatol.* **2014**, *34*, 3001–3023. [[CrossRef](#)]
23. de Oliveira-Júnior, J.F.; de Gois, G.; de Bodas Terassi, P.M.; da Silva, C.A., Jr.; Blanco, C.J.C.; Sobral, B.S.; Gasparini, K.A.C. Drought severity based on the SPI index and its relation to the ENSO and PDO climatic variability modes in the regions North and Northwest of the State of Rio de Janeiro-Brazil. *Atmos. Res.* **2018**, *212*, 91–105. [[CrossRef](#)]
24. Brito, S.S.B.; Cunha, A.P.M.A.; Cunningham, C.C.; Alvalá, R.C.; Marengo, J.A.; Carvalho, M.A. Frequency, duration and severity of drought in the Semiarid Northeast Brazil region. *Int. J. Climatol.* **2018**, *38*, 517–529. [[CrossRef](#)]
25. Huete, A.; Justice, C.; Liu, H. Development of vegetation and soil indices for MODIS-EOS. *Remote Sens. Environ.* **1994**, *49*, 224–234. [[CrossRef](#)]
26. Brando, P.M.; Goetz, S.J.; Baccini, A.; Nepstad, D.C.; Beck, P.S.A.; Christman, M.C. Seasonal and interannual variability of climate and vegetation indices across the Amazon. *Proc. Natl. Acad. Sci. USA* **2010**, *107*, 14685–14690. [[CrossRef](#)] [[PubMed](#)]
27. Fung, K.F.; Huang, Y.F.; Koo, C.H. Assessing drought conditions through temporal pattern, spatial characteristic and operational accuracy indicated by SPI and SPEI: Case analysis for Peninsular Malaysia. *Nat. Hazards* **2020**, *103*, 2071–2101. [[CrossRef](#)]
28. Vicente-Serrano, S.M.; Beguería, S.; López-Moreno, J.I. A Multiscalar Drought Index Sensitive to Global Warming: The Standardized Precipitation Evapotranspiration Index. *J. Clim.* **2010**, *23*, 1696–1718. [[CrossRef](#)]
29. Spinoni, J.; Barbosa, P.; De Jager, A.; McCormick, N.; Naumann, G.; Vogt, J.V.; Magni, D.; Masante, D.; Mazzeschi, M. A new global database of meteorological drought events from 1951 to 2016. *J. Hydrol. Reg. Stud.* **2019**, *22*, 100593. [[CrossRef](#)]
30. Bezdan, J.; Bezdan, A.; Blagojević, B.; Mesaroš, M.; Pejić, B.; Vranešević, M.; Pavić, D.; Nikolić-Đorić, E. SPEI-Based Approach to Agricultural Drought Monitoring in Vojvodina Region. *Water* **2019**, *11*, 1481. [[CrossRef](#)]
31. Karnieli, A.; Agam, N.; Pinker, R.T.; Anderson, M.; Imhoff, M.L.; Gutman, G.G.; Panov, N.; Goldberg, A. Use of NDVI and Land Surface Temperature for Drought Assessment: Merits and Limitations. *J. Clim.* **2010**, *23*, 618–633. [[CrossRef](#)]
32. Huete, A.; Didan, K.; Miura, T.; Rodriguez, E.; Gao, X.; Ferreira, L. Overview of the radiometric and biophysical performance of the MODIS vegetation indices. *Remote Sens. Environ.* **2002**, *83*, 195–213. [[CrossRef](#)]
33. Huete, A.R.; Liu, H.; van Leeuwen, W.J.D. The use of vegetation indices in forested regions: Issues of linearity and saturation. In *Proceedings of the 1997 IEEE International Geoscience and Remote Sensing Symposium Proceedings, Remote Sensing—A Scientific Vision for Sustainable Development, IGARSS '97, Singapore, 3–8 August 1997; Volume 4, pp. 1966–1968.*
34. Marengo, J.; Nobre, C.; Tomasella, J.; Cardoso, M.; Oyama, M. Hydro-climatic and ecological behaviour of the drought of Amazonia in 2005. *Philos. Trans. R. Soc. B Biol. Sci.* **2008**, *363*, 1773–1778. [[CrossRef](#)]
35. Marengo, J.A.; Alves, L.M.; Alvalá, R.; Cunha, A.P.; Brito, S.; Moraes, O.L.L.L. Climatic characteristics of the 2010–2016 drought in the semiarid Northeast Brazil region. *An. Acad. Bras. Cienc.* **2018**, *90*, 1973–1985. [[CrossRef](#)] [[PubMed](#)]
36. Asner, G.P.; Alencar, A. Drought impacts on the Amazon forest: The remote sensing perspective. *New Phytol.* **2010**, *187*, 569–578. [[CrossRef](#)] [[PubMed](#)]

37. Atkinson, P.M.; Dash, J.; Jeganathan, C. Amazon vegetation greenness as measured by satellite sensors over the last decade. *Geophys. Res. Lett.* **2011**, *38*, L19105. [[CrossRef](#)]
38. Anderson, L.O.; Malhi, Y.; Aragao, L.E.O.C.; Saatchi, S. Spatial patterns of the canopy stress during 2005 drought in Amazonia. In Proceedings of the 2007 IEEE International Geoscience and Remote Sensing Symposium, Barcelona, Spain, 23–27 July 2007; pp. 2294–2297.
39. Xu, L.; Samanta, A.; Costa, M.H.; Ganguly, S.; Nemani, R.R.; Myneni, R.B. Widespread decline in greenness of Amazonian vegetation due to the 2010 drought. *Geophys. Res. Lett.* **2011**, *38*, L07402. [[CrossRef](#)]
40. Sorí, R.; Marengo, J.; Nieto, R.; Drumond, A.; Gimeno, L. Drought and wet episodes in Amazonia: The role of atmospheric moisture transport. In *Proceedings of the First International Electronic Conference on the Hydrological Cycle*; MDPI: Basel, Switzerland, 2017; Volume 1, p. 4846.
41. Drumond, A.; Stojanovic, M.; Nieto, R.; Vicente-Serrano, S.M.; Gimeno, L. Linking Anomalous Moisture Transport And Drought Episodes in the IPCC Reference Regions. *Bull. Am. Meteorol. Soc.* **2019**, *100*, 1481–1498. [[CrossRef](#)]
42. Harris, I.; Jones, P.D.; Osborn, T.J.; Lister, D.H. Updated high-resolution grids of monthly climatic observations—The CRU TS3.10 Dataset. *Int. J. Climatol.* **2014**, *34*, 623–642. [[CrossRef](#)]
43. Labat, D.; Ronchail, J.; Callede, J.; Guyot, J.L.; De Oliveira, E.; Guimarães, W. Wavelet analysis of Amazon hydrological regime variability. *Geophys. Res. Lett.* **2004**, *31*, 3–6. [[CrossRef](#)]
44. Botto, M.P. The Amazon Cooperation Treaty: A mechanism for cooperation and sustainable. In *Management of Latin American River Basins: Amazon, Plata, and Sao Francisco*; Biswas, A.K., Cordeiro, N.V., Braga, B.P.F., Tortajada, C., Eds.; United Nations University Press: Tokyo, Japan, 1999; p. 68. ISBN 9789280810127.
45. Lees, A.C.; Peres, C.A.; Fearnside, P.M.; Schneider, M.; Zuanon, J.A.S. Hydropower and the future of Amazonian biodiversity. *Biodivers. Conserv.* **2016**, *25*, 451–466. [[CrossRef](#)]
46. Beck, H.E.; Zimmermann, N.E.; McVicar, T.R.; Vergopolan, N.; Berg, A.; Wood, E.F. Present and future Köppen-Geiger climate classification maps at 1-km resolution. *Sci. Data* **2018**, *5*, 180214. [[CrossRef](#)]
47. Coe, M.T.; Macedo, M.N.; Brando, P.M.; Lefebvre, P.; Panday, P.; Silvério, D. The Hydrology and Energy Balance of the Amazon Basin. In *Interactions Between Biosphere, Atmosphere and Human Land Use in the Amazon Basin*; Springer: Cham, Switzerland, 2016; pp. 35–53.
48. Marengo, J.A. Interdecadal variability and trends of rainfall across the Amazon basin. *Theor. Appl. Climatol.* **2004**, *78*, 79–96. [[CrossRef](#)]
49. Marengo, J.A. Interannual variability of surface climate in the Amazon basin. *Int. J. Climatol.* **1992**, *12*, 853–863. [[CrossRef](#)]
50. Marengo, J.A.; Alves, L.M.; Soares, W.R.; Rodriguez, D.A.; Camargo, H.; Riveros, M.P.; Pabló, A.D. Two Contrasting Severe Seasonal Extremes in Tropical South America in 2012: Flood in Amazonia and Drought in Northeast Brazil. *J. Clim.* **2013**, *26*, 9137–9154. [[CrossRef](#)]
51. Lima, L.S.; Coe, M.T.; Filho, B.S.S.; Cuadra, S.V.; Dias, L.C.P.; Costa, M.H.; Lima, L.S.; Rodrigues, H.O. Feedbacks between deforestation, climate, and hydrology in the Southwestern Amazon: Implications for the provision of ecosystem services. *Landsc. Ecol.* **2014**, *29*, 261–274. [[CrossRef](#)]
52. Mayorga, E.; Logsdon, M.G.; Ballester, M.V.R.; Richey, J.E. Estimating cell-to-cell land surface drainage paths from digital channel networks, with an application to the Amazon basin. *J. Hydrol.* **2005**, *315*, 167–182. [[CrossRef](#)]
53. Kumar, S.; Vidal, Y.-S.; Moya-Álvarez, A.S.; Martínez-Castro, D. Effect of the surface wind flow and topography on precipitating cloud systems over the Andes and associated Amazon basin: GPM observations. *Atmos. Res.* **2019**, *225*, 193–208. [[CrossRef](#)]
54. Liu, X.; Yu, L.; Si, Y.; Zhang, C.; Lu, H.; Yu, C.; Gong, P. Identifying patterns and hotspots of global land cover transitions using the ESA CCI Land Cover dataset. *Remote Sens. Lett.* **2018**, *9*, 972–981. [[CrossRef](#)]
55. Funk, C.; Peterson, P.; Landsfeld, M.; Pedreros, D.; Verdin, J.; Shukla, S.; Husak, G.; Rowland, J.; Harrison, L.; Hoell, A.; et al. The climate hazards infrared precipitation with stations—A new environmental record for monitoring extremes. *Sci. Data* **2015**, *2*, 150066. [[CrossRef](#)] [[PubMed](#)]
56. Berry, P.A.M.; Garlick, J.D.; Smith, R.G. Near-global validation of the SRTM DEM using satellite radar altimetry. *Remote Sens. Environ.* **2007**, *106*, 17–27. [[CrossRef](#)]
57. Allen, R.G.; Pereira, L.S.; Raes, D.; Smith, M. Crop evapotranspiration—Guidelines for computing crop water requirements—FAO Irrigation and drainage paper 56. *FAO (Rome)* **1998**, *300*, D05109.
58. Harris, I.; Osborn, T.J.; Jones, P.; Lister, D. Version 4 of the CRU TS monthly high-resolution gridded multivariate climate dataset. *Sci. Data* **2020**, *7*, 109. [[CrossRef](#)]
59. Solano, R.; Didan, K.; Jacobson, A.; Huete, A. *MODIS Vegetation Index User's Guide (MOD13 Series)*; Veg. Index Phenol. Lab, Univ. Arizona: Tucson, AZ, USA, 2010; pp. 1–38.
60. Jäntschi, L. A Test Detecting the Outliers for Continuous Distributions Based on the Cumulative Distribution Function of the Data Being Tested. *Symmetry* **2019**, *11*, 835.
61. McKnight, P.E.; McKnight, K.M.; Sidani, S.; Figueredo, A.J. *Missing Data: A Gentle Introduction*; Guilford Press: New York, NY, USA, 2007; ISBN 9781606238202.
62. Moritz, S.; Bartz-Beielstein, T. ImputeTS: Time series missing value imputation in R. *R J.* **2017**, *9*, 207–218. [[CrossRef](#)]



63. Dee, D.P.; Uppala, S.M.; Simmons, A.J.; Berrisford, P.; Poli, P.; Kobayashi, S.; Andrae, U.; Balmaseda, M.A.; Balsamo, G.; Bauer, P.; et al. The ERA-Interim reanalysis: Configuration and performance of the data assimilation system. *Q. J. R. Meteorol. Soc.* **2011**, *137*, 553–597. [[CrossRef](#)]
64. Houghton, R.A.; Bontemps, S.; Peng, S.; Lamarche, C.; Li, W.; MacBean, N.; Defourny, P.; Ciais, P. Gross and net land cover changes based on plant functional types derived from the annual ESA CCI land cover maps. *Earth Syst. Sci. Data Discuss.* **2017**, *10*, 1–23.
65. Melo, D.C.D.; Xavier, A.C.; Bianchi, T.; Oliveira, P.T.S.; Scanlon, B.R.; Lucas, M.C.; Wendland, E. Performance evaluation of rainfall estimates by TRMM Multi-satellite Precipitation Analysis 3B42V6 and V7 over Brazil. *J. Geophys. Res. Atmos.* **2015**, *120*, 9426–9436. [[CrossRef](#)]
66. Pellicone, G.; Caloiero, T.; Modica, G.; Guagliardi, I. Application of several spatial interpolation techniques to monthly rainfall data in the Calabria region (southern Italy). *Int. J. Climatol.* **2018**, *38*, 3651–3666. [[CrossRef](#)]
67. Stagge, J.H.; Tallaksen, L.M.; Gudmundsson, L.; Van Loon, A.F.; Stahl, K. Candidate Distributions for Climatological Drought Indices (SPI and SPEI). *Int. J. Climatol.* **2015**, *35*, 4027–4040. [[CrossRef](#)]
68. Levine, R.A.; Wilks, D.S. Statistical Methods in the Atmospheric Sciences. *J. Am. Stat. Assoc.* **2000**, *95*, 344. [[CrossRef](#)]
69. Yue, S.; Wang, C. The Mann-Kendall Test Modified by Effective Sample Size to Detect Trend in Serially Correlated Hydrological Series. *Water Resour. Manag.* **2004**, *18*, 201–218. [[CrossRef](#)]
70. Hu, Z.; Liu, S.; Zhong, G.; Lin, H.; Zhou, Z. Modified Mann-Kendall trend test for hydrological time series under the scaling hypothesis and its application. *Hydrol. Sci. J.* **2020**, *65*, 2419–2438. [[CrossRef](#)]
71. Theil, H. A Rank-Invariant Method of Linear and Polynomial Regression Analysis. In *Henri Theil's Contributions to Economics and Econometrics*; Springer: Cham, Switzerland, 1992; pp. 345–381.
72. Ghaderpour, E.; Ince, E.S.; Pagiatakis, S.D. Least-squares cross-wavelet analysis and its applications in geophysical time series. *J. Geod.* **2018**, *92*, 1223–1236. [[CrossRef](#)]
73. Torrence, C.; Compo, G.P. A Practical Guide to Wavelet Analysis. *Bull. Am. Meteorol. Soc.* **1998**, *79*, 61–78. [[CrossRef](#)]
74. Grinsted, A.; Moore, J.C.; Jevrejeva, S. Application of the cross wavelet transform and wavelet coherence to geophysical time series. *Nonlinear Process. Geophys.* **2004**, *11*, 561–566. [[CrossRef](#)]
75. Park, H.-S.; Jun, C.-H. A simple and fast algorithm for K-medoids clustering. *Expert Syst. Appl.* **2009**, *36*, 3336–3341. [[CrossRef](#)]
76. Arora, P.; Deepali, D.; Varshney, S. Analysis of k-means and k-medoids algorithm for big data. *Procedia Comput. Sci.* **2016**, *78*, 507–512. [[CrossRef](#)]
77. Reynolds, A.P.; Richards, G.; de la Iglesia, B.; Rayward-Smith, V.J. Clustering Rules: A Comparison of Partitioning and Hierarchical Clustering Algorithms. *J. Math. Model. Algorithms* **2006**, *5*, 475–504. [[CrossRef](#)]
78. Kayano, M.T.; Andreoli, R.V.; Souza, R.A.F. Pacific and Atlantic multidecadal variability relations to the El Niño events and their effects on the South American rainfall. *Int. J. Climatol.* **2020**, *40*, 2183–2200. [[CrossRef](#)]
79. Barbosa, H.A.; Kumar, T.V.L. Influence of rainfall variability on the vegetation dynamics over Northeastern Brazil. *J. Arid Environ.* **2016**, *124*, 377–387. [[CrossRef](#)]
80. Rossato, L.; Marengo, J.A.; de Angelis, C.F.; Pires, L.B.M.; Mendonça, E.M. Impact of soil moisture over Palmer Drought Severity Index and its future projections in Brazil. *RBRH* **2017**, *22*, e36. [[CrossRef](#)]
81. Mbatha, N.; Xulu, S. Time Series Analysis of MODIS-Derived NDVI for the Hluhluwe-Imfolozi Park, South Africa: Impact of Recent Intense Drought. *Climate* **2018**, *6*, 95. [[CrossRef](#)]
82. Zhao, W.; Zhao, X.; Zhou, T.; Wu, D.; Tang, B.; Wei, H. Climatic factors driving vegetation declines in the 2005 and 2010 Amazon droughts. *PLoS ONE* **2017**, *12*, e0175379. [[CrossRef](#)] [[PubMed](#)]
83. Van Loon, A.F. Hydrological drought explained. *Wiley Interdiscip. Rev. Water* **2015**, *2*, 359–392. [[CrossRef](#)]
84. Van Loon, A.F.; Laaha, G. Hydrological drought severity explained by climate and catchment characteristics. *J. Hydrol.* **2015**, *526*, 3–14. [[CrossRef](#)]
85. Esteban, E.J.L.; Castilho, C.V.; Melgaço, K.L.; Costa, F.R.C. The other side of droughts: Wet extremes and topography as buffers of negative drought effects in an Amazonian forest. *New Phytol.* **2020**, *229*, 1995–2006. [[CrossRef](#)]
86. Sheffield, J. *Drought*; Routledge: Abingdon, UK, 2012; ISBN 9781849775250.
87. Marengo, J.A.; Williams, E.R.; Alves, L.M.; Soares, W.R.; Rodriguez, D.A. Extreme Seasonal Climate Variations in the Amazon Basin: Droughts and Floods. In *Interactions between Biosphere, Atmosphere and Human Land Use in the Amazon Basin*; Springer: Cham, Switzerland, 2016; pp. 55–76.
88. Satyamurty, P.; da Costa, C.P.W.; Manzi, A.O. Moisture source for the Amazon Basin: A study of contrasting years. *Theor. Appl. Climatol.* **2013**, *111*, 195–209. [[CrossRef](#)]
89. De Souza, E.B.; Ambrizzi, T. Modulation of the intraseasonal rainfall over tropical Brazil by the Madden-Julian oscillation. *Int. J. Climatol.* **2006**, *26*, 1759–1776. [[CrossRef](#)]
90. Andreoli, R.V.; de Souza, R.A.F.; Kayano, M.T.; Candido, L.A. Seasonal anomalous rainfall in the central and eastern Amazon and associated anomalous oceanic and atmospheric patterns. *Int. J. Climatol.* **2012**, *32*, 1193–1205. [[CrossRef](#)]
91. Bagley, J.E.; Desai, A.R.; Harding, K.J.; Snyder, P.K.; Foley, J.A. Drought and Deforestation: Has Land Cover Change Influenced Recent Precipitation Extremes in the Amazon? *J. Clim.* **2014**, *27*, 345–361. [[CrossRef](#)]
92. Awange, J.L.; Mpelasoka, F.; Goncalves, R.M. When every drop counts: Analysis of Droughts in Brazil for the 1901–2013 period. *Sci. Total Environ.* **2016**, *566–567*, 1472–1488. [[CrossRef](#)]

93. Chaudhari, S.; Pokhrel, Y.; Moran, E.; Miguez-Macho, G. Multi-decadal hydrologic change and variability in the Amazon River basin: Understanding terrestrial water storage variations and drought characteristics. *Hydrol. Earth Syst. Sci.* **2019**, *23*, 2841–2862. [[CrossRef](#)]
94. Kayano, M.T.; Capistrano, V.B. How the Atlantic multidecadal oscillation (AMO) modifies the ENSO influence on the South American rainfall. *Int. J. Climatol.* **2014**, *34*, 162–178. [[CrossRef](#)]
95. Kayano, M.T.; Andreoli, R.V. Relations of South American summer rainfall interannual variations with the Pacific Decadal Oscillation. *Int. J. Climatol.* **2007**, *27*, 531–540. [[CrossRef](#)]
96. Espinoza, J.C.; Ronchail, J.; Marengo, J.A.; Segura, H. Contrasting North–South changes in Amazon wet-day and dry-day frequency and related atmospheric features (1981–2017). *Clim. Dyn.* **2019**, *52*, 5413–5430. [[CrossRef](#)]
97. Nogueira, J.; Rambal, S.; Barbosa, J.; Mouillot, F. Spatial Pattern of the Seasonal Drought/Burned Area Relationship across Brazilian Biomes: Sensitivity to Drought Metrics and Global Remote-Sensing Fire Products. *Climate* **2017**, *5*, 42. [[CrossRef](#)]
98. da Silva, S.S.; Fearnside, P.M.; de Alencastro Graça, P.M.L.; Brown, I.F.; Alencar, A.; de Melo, A.W.F. Dynamics of forest fires in the southwestern Amazon. *For. Ecol. Manag.* **2018**, *424*, 312–322. [[CrossRef](#)]
99. Lopes, A.V.; Chiang, J.C.H.; Thompson, S.A.; Dracup, J.A. Trend and uncertainty in spatial-temporal patterns of hydrological droughts in the Amazon basin. *Geophys. Res. Lett.* **2016**, *43*, 3307–3316. [[CrossRef](#)]